

SPECTROSCOPIC CONFIRMATION OF AN ULTRA MASSIVE AND COMPACT GALAXY AT $Z=3.35$: A DETAILED LOOK AT AN EARLY PROGENITOR OF LOCAL MOST MASSIVE ELLIPTICALS

Z. CEMILE MARSAN¹, DANILO MARCHESINI¹, GABRIEL B. BRAMMER², MAURO STEFANON³, ADAM MUZZIN⁴, ALBERTO FERNÁNDEZ-SOTO^{5,6}, KEVIN N. HAINLINE⁷, IVO LABBÉ⁴, SUNE TOFT⁸, PIETER G. VAN DOKKUM⁹

To be submitted to the Astrophysical Journal

ABSTRACT

We present the first spectroscopic confirmation of an ultra-massive galaxy at redshift $z > 3$ using data from Keck-NIRSPEC, VLT-Xshooter, and GTC-Osiris. We detect strong [OIII] and Ly α emission, and weak [OII], CIV, and HeII, placing C1-23152 at a spectroscopic redshift of $z_{spec} = 3.351$. The modeling of the emission-line corrected spectral energy distribution results in a best-fit stellar mass of $M_* = 3.1^{+0.6}_{-0.7} \times 10^{11} M_\odot$, a star-formation rate of $< 7 M_\odot \text{ yr}^{-1}$, and negligible dust extinction. The stars appear to have formed in a short intense burst $\sim 300\text{-}500$ Myr prior to the observation epoch, setting the formation redshift of this galaxy at $z \sim 4.1$. From the analysis of the line ratios and widths, and the observed flux at $24 \mu\text{m}$, we confirm the presence of a luminous hidden active galactic nucleus (AGN), with bolometric luminosity of $\sim 10^{46} \text{ erg s}^{-1}$. Potential contamination to the observed SED from the AGN continuum is constrained, placing a lower limit on the stellar mass of $2 \times 10^{11} M_\odot$. HST/WFC3 H₁₆₀ and ACS I₈₁₄ images are modeled, resulting in an effective radius of $r_e \sim 1$ kpc in the H₁₆₀ band and a Sérsic index $n \sim 4.4$. This object may be a prototype of the progenitors of local most massive elliptical galaxies in the first 2 Gyr of cosmic history, having formed most of its stars at $z > 4$ in a highly dissipative, intense, and short burst of star formation. C1-23152 is completing its transition to a post-starburst phase while hosting a powerful AGN, potentially responsible for the quenching of the star formation activity.

Subject headings: cosmology: observations — galaxies: evolution — galaxies: formation — galaxies: fundamental parameters — galaxies: high-redshift — galaxies: stellar content — infrared: galaxies — galaxies: structure — galaxies: active — galaxies: individual

1. INTRODUCTION

One of the most fundamental questions regarding galaxy formation and evolution is when and how the most massive galaxies in the universe formed. In the current Λ CDM paradigm, the dominant structures in the universe are dark matter haloes that grow out of primordial density perturbations through gravitational collapse (White & Rees 1978). Simulations and analytical models establish that this process proceeds in a hierarchical, bottom-up manner with low mass haloes forming first and subsequently growing by continued accretion and merging to form more massive haloes at later times (White & Frenk 1991; Kauffmann & White 1993; Kauffmann et al. 1999). In contrast, observational studies suggest that the stellar baryonic component of haloes assemble in an anti-hierarchical, top-down manner (Cowie et al. 1996; Fontanot et al. 2009).

Closely related to this issue is the intriguing finding that the number density of the most massive galaxies ($M_* > 3 \times$

$10^{11} M_\odot$) seems to evolve very little from $z \sim 4$ to $z \sim 1.5$ (Perez-Gonzalez et al. 2008; Marchesini et al. 2009, 2010; Muzzin et al. 2013b), suggesting that very massive galaxies were already in place at $z \sim 3.5$, and implying that their stellar content was assembled rapidly in the first ~ 1.5 Gyr of cosmic history. Whereas theoretical models of galaxy formation and evolution severely under-predict the observed number density of galaxies at $3 < z < 4$ with $\log(M_*/M_\odot) > 11.5$ (Fontanot et al. 2009; Marchesini et al. 2009, 2010), systematic uncertainties in both photometric redshifts and stellar mass estimates remain large, with no spectroscopically confirmed very massive galaxies at $z > 3$.

An additional tension between observations and model predictions is represented by the small sizes of massive quiescent galaxies at $z \sim 2$. Specifically, among massive galaxies (e.g., $M_* > 10^{11} M_\odot$) at $z \sim 2$, approximately 40% are no longer forming stars (Whitaker et al. 2011; Brammer et al. 2011; Muzzin et al. 2013b). Surprisingly, these massive quiescent galaxies have been found to be compact, particularly those with the lowest star formation rates, with sizes a factor of $\sim 4\text{-}5x$ smaller at $z \sim 2$ compared to local quiescent galaxies with similar stellar masses (Daddi et al. 2005; Trujillo et al. 2006; Toft et al. 2007; Trujillo et al. 2007; Zirm et al. 2007; Cimatti et al. 2008; van Dokkum et al. 2008; Franx et al. 2008; van der Wel et al. 2008; Bezanson et al. 2009; van Dokkum et al. 2010; see van der Wel et al. 2014 for the latest comprehensive analysis on the size evolution of quiescent and star-forming galaxies). It has been suggested that dry minor mergers can cause a considerable growth in size without significantly increasing the mass of the galaxy, whereas major mergers tend to increase the mass without increasing the size much (Naab et al. 2006; Trujillo et al. 2011). A consistent size evolution through mi-

¹ Department of Physics and Astronomy, Tufts University, Medford, MA 02155, USA

² Space Telescope Science Institute, 3700 San Martin Drive, Baltimore, MD 21218, USA

³ Physics and Astronomy Department, University of Missouri, Columbia, MO 65211, USA

⁴ Leiden Observatory, Leiden University, PO Box 9513, NL-2300 RA Leiden, The Netherlands

⁵ Instituto de Física de Cantabria (CSIC-Universidad de Cantabria), Avda. de los Castros s/n, 39005-Santander, Spain

⁶ Unidad Asociada Observatori Astronòmic (IFCA-Universitat de València), C. Catedrático José Beltrán 2, 46980-Paterna, Spain

⁷ Department of Physics and Astronomy, Dartmouth College, Hanover, NH 03755, USA

⁸ Dark Cosmology Centre, Niels Bohr Institute, University of Copenhagen, Juliane Maries Vej 30, DK-2100 Copenhagen, Denmark

⁹ Department of Astronomy, Yale University, New Haven, CT 06511, USA

nor merging can be achieved as less massive satellite galaxies deposit mass preferentially in the outer radii of more massive central galaxies (commonly referred to as *inside-out growth*). Several recent works have indeed shown that the mass at fixed inner physical radius of massive, quiescent galaxies is nearly constant, whereas the mass in the outer regions undergoes a significant increase (a factor of ~ 4 since $z \sim 2$), supporting the inside-out growth of massive, quiescent galaxies (e.g., van Dokkum et al. 2010; Van De Sande et al. 2013; Patel et al. 2013).

In order to understand the onset and evolution of massive galaxies, several recent works have aimed at identifying the potential progenitors of compact, massive quiescent galaxies observed at $z \sim 2$, based on number density considerations (Barro et al. 2013; Stefanon et al. 2013; Patel et al. 2013; Williams et al. 2014). Two evolutionary tracks have been proposed for the formation of massive, quiescent galaxies: an early ($z > 2$) formation path of rapidly quenched compact star-forming galaxies fading into compact, quiescent galaxies that later enlarge within the quiescent phase; and a late-arrival ($z < 2$) path in which quiescent galaxies are formed through the quenching of more extended star-forming galaxies with lower mass densities (Barro et al. 2013).

Most recently, Marchesini et al. (2014) studied the evolution of the properties of the progenitors of ultra-massive galaxies ($\log(M_*/M_\odot) \approx 11.8$; UMGs) at $z \sim 0$ with a semi-empirical approach using abundance matching. At $2 < z < 3$, the progenitors of local UMGs are found to be dominated by massive ($M_* \approx 2 \times 10^{11} M_\odot$), dusty ($A_V \sim 1-2.2$ mag), and star forming ($\text{SFR} \sim 100-400 M_\odot \text{yr}^{-1}$) galaxies, although a small fraction ($\sim 15\%$) of them are found to be already quiescent at $2.5 < z < 3.0$. The $2.5 < z < 3.0$ quiescent progenitors of local UMGs are found to have properties typical of young (0.6-1 Gyr) post-starburst galaxies with little dust extinction ($A_V \sim 0.4$ mag) and strong Balmer breaks, showing a large scatter in rest-frame $U-V$ color (~ 0.2 mag). The existence of such quiescent progenitors at $z = 2.75$ indicates that the early assembly of the massive end of the local quiescent red-sequence must have started at $z > 3$, as also implied by archeological studies in the local universe (e.g., Thomas et al. 2005; Gallazzi et al. 2006; Thomas et al. 2010).

Evidence for the existence of massive ($M_* > 10^{11}$) galaxies at $z > 3$ with suppressed star formation has been found through studies of deep near-infrared selected catalogs (Wiklind et al. 2008; Mancini et al. 2009; Marchesini et al. 2010; Stefanon et al. 2013; Muzzin et al. 2013b; Straatman et al. 2014), with accurate photometric redshifts and well-sampled SEDs. However, spectroscopic observations are necessary to confirm the redshifts and to better characterize the properties of these galaxies. It is also of vital importance to determine AGN and/or starburst contamination to the optical-to-MIR SEDs of these sources to properly constrain the high-mass end of the stellar mass function at these redshifts.

In this paper, we present the first spectroscopic confirmation of a very massive galaxy at $z > 3$, C1-23152, with a detailed investigation of its stellar population and structural properties, as well as the AGN energetics. C1-23152 is the brightest ($K = 20.3$ mag, AB) galaxy within the stellar mass complete ($M_* > 2.5 \times 10^{11} M_\odot$) sample of 14 galaxies at $3 < z < 4$ presented in Marchesini et al. (2010) was initially selected from the NEWFIRM Medium-Band Survey (NMBS; Whitaker et al. 2011). C1-23152 is in the COSMOS field (Scoville et al. 2007), and has a photometric red-

shift $z_{\text{phot}} = 3.29 \pm 0.06$ and a stellar mass of $\log(M_*/M_\odot) = 11.42$ (Marchesini et al. 2010). By combining the broad- and medium-band photometry from NMBS with optical and near-infrared (NIR) spectroscopic data from both ground- and space-based facilities, we spectroscopically confirm the very large stellar mass of C1-23152 through detailed modeling of its spectral energy distribution (SED), and provide robust evidence for the evolutionary path linking C1-23152 to local giant elliptical galaxies.

This paper is organized as follows: In §2, we present the observations of C1-23152, including extensive space- and ground-based spectroscopy from the ultra-violet (UV) to the near-infrared (NIR), as well as space-based imaging. In §3, we present the analysis of the spectra and the modeling of the SED, and the derivation of the structural parameters from space-based imaging. The results are summarized and discussed in §4. We assume $\Omega_M = 0.3$, $\Omega_\Lambda = 0.7$, $H_0 = 70 \text{ km s}^{-1} \text{ Mpc}^{-1}$, and a Kroupa (2001) initial mass function (IMF) throughout the paper. All magnitudes are on the AB system.

2. DATA

2.1. Broad- and medium-band photometry from the NMBS

The target C1-23152 (RA=10^h00^m27^s.81, DEC=+02^d33^m49^s.3; J2000) is selected from the mass-complete ($M_* > 2.5 \times 10^{11} M_\odot$) sample of galaxies at $3 < z < 4$ constructed from the NMBS and presented in Marchesini et al. (2010). C1-23152 lies in the COSMOS field (Scoville et al. 2007), with excellent supporting data. The NMBS photometry presented in Whitaker et al. (2011) includes deep optical *ugriz* data from the CFHT Legacy Survey, deep *Spitzer-IRAC* and MIPS imaging (Sanders et al. 2007), deep Subaru images with the $B_J V_J r^+ i^+ z^+$ broadband filters (Capak et al. 2007), Subaru images with 12 optical intermediate-band filters from 427 to 827 nm (Taniguchi et al. 2007), *JHK_S* broadband imaging from the WIRCam Deep Survey (WIRDS; McCracken et al. 2010), *Galaxy Evolution Explorer (GALEX)* photometry in the FUV (150 nm) and NUV (225 nm) passbands (Martin et al. 2005), and NIR imaging with NEWFIRM using the five medium-band filters J_1, J_2, J_3, H_1, H_2 , and broad-band K from NMBS (van Dokkum et al. 2009), for a total of 37 photometric points. In the publicly released v5.1 NMBS catalog, C1-23152 is identified as C1-35502, and has total apparent magnitudes of $K_S = 20.31$ mag and $r = 23.24$ mag.

2.2. Ground-based spectroscopy and data reduction

In this section we describe the ground-based spectroscopic data of C1-23152 obtained from Keck-NIRSPEC, VLT-Xshooter, and GTC-Osiris as part of follow-up programs aimed at spectroscopically confirming the existence of very massive galaxies at $z > 3$. Along with the observational techniques, we provide a summary of the data reduction. The detailed description of the data reduction and the full sample will be presented elsewhere (C. Marsan et al. 2014; in preparation). Table 1 summarizes the wavelength coverage, total exposure time, seeing, date of observations, and the slit width of the spectroscopic observations.

2.2.1. Keck-NIRSPEC

We observed C1-23152 using Keck-NIRSPEC (McLean et al. 1998) in cross-dispersed mode and the $42'' \times 0.76''$ slit for both N5 (H) and N7 (K) filters, obtaining

TABLE 1. GROUND-BASED SPECTROSCOPIC OBSERVATIONS

Band/Arm	λ_{range} (μ)	t_{exp} (min)	FWHM ($''$)	Date	Width ($''$)
<i>Keck-NIRSPEC</i>					
N5 (H)	1.48 - 1.71	75	0.7	11 Feb 2011	0.72
N7 (K)	1.94 - 2.37	75	0.7	11 Feb 2011	0.72
<i>VLT-Xshooter</i>					
UVB	0.3 - 0.59	35	1.16	27 May 2011	1.0
VIS	0.53 - 1.02	35	1.16	27 May 2011	0.9
NIR	0.99 - 2.48	40	1.16	27 May 2011	0.9
<i>GTC-Osiris</i>					
R1000B	0.37 - 0.77	42	0.9	Nov 2011	0.8
R1000B	0.37 - 0.77	42	1.6	Feb 2012	0.8
R1000B	0.37 - 0.77	45	1.0	Jan 2013	0.8

NOTE. — λ_{range} is the wavelength range covered by the instrumental setup; t_{exp} is the on-source exposure time in minutes; FWHM is the average seeing in arcsec of the observations. The last two columns list the nights during which the spectroscopic data were taken and the width of the used slit in arcsec, respectively.

a wavelength coverage of 1.48-1.71 μm and 1.94-2.37 μm , and a spectral resolution of $R=1100$ and $R=1500$, respectively. The observations were carried out on the night of February 11, 2011 as part of the NOAO program 2011A-0514 (PI: Marchesini) with a typical seeing of 0.7 $''$ which worsened throughout the sequence of observations due to cloudy variable weather. Observations were conducted following an ABA/B' on-source dither pattern. The orientation of the slit was set to include a bright point source to serve as reference when analyzing and combining the two dimensional rectified frames. The target was acquired using blind offsets from a nearby bright star. The alignment of the offset star in the slit was checked before each individual 900 sec exposure and corrected when necessary. Before and after the observing sequence, a spectrophotometric standard and an AV0 star was observed for the purpose of correcting for telluric absorption and detector response.

The data reduction for the NIRSPEC observations used a combination of custom IDL scripts and standard IRAF tasks¹⁰. As the initial step, a bad pixel mask was created by flagging outlier pixels in dark and flat frames. The cosmic rays on the science frames were removed using L.A.Cosmic (van Dokkum 2001). The frames and their corresponding sky spectra were rotated such that the sky lines are along columns, using a polynomial to interpolate between adjacent pixels. The spectra were wavelength calibrated by fitting Gaussian profiles to the OH lines in the 2D sky spectra. Each spectrum was sky subtracted using an adjacent spectrum with the IDL routines written by George Becker. The sky subtracted frames and the sky spectra were rectified to a linear wavelength scale. The standard star frames used to correct for atmospheric absorption and detector response were rectified and reduced in the same manner as the science frames. A one-dimensional spectrum was extracted for each telluric standard star (before and after science observations) by summing all the rows (along the spatial direction) with a flux greater than 0.1 times that of the central row. The average of the one-dimensional telluric star spectra was used to correct the two dimensional

science and spectrophotometric star frames for telluric absorption. The one-dimensional spectrum of the spectrophotometric star was extracted in the same manner, and used to create a response function for flux calibration. The two dimensional rectified and reduced science frames were combined by weighting according to their signal-to-noise ratio (S/N).

2.2.2. VLT-Xshooter

Xshooter is a single-object, medium-resolution echelle spectrograph with simultaneous coverage of wavelength range 0.3-2.5 μm in three arms (UVB, VIS, NIR) (D'Odorico et al. 2006). The observations of our target were carried out in queue mode as part of the ESO program 087.A-0514 (PI: Brammer) under poor seeing conditions (FWHM \sim 1.2 $''$), following an ABA/B' on-source dither pattern using the 11 $''\times$ 1.0 $''$ and 11 $''\times$ 0.9 $''$ slits for the UVB and VIS/NIR arms, respectively. This instrumental setup resulted in a spectral resolution of $R=4200$, 8250, and 4000 for the NIR, VIS and UVB arms, respectively. Telluric and spectrophotometric standard stars were observed in the same setup as science observations for calibration purposes.

The data reduction for the Xshooter observations used custom scripts based on the standard Xshooter reduction pipeline (Modigliani et al. 2010). The calibration steps (master darks, order prediction, flat fields, and the two-dimensional maps for later rectification of the spectra) were run with the default parameters in the pipeline (Goldoni 2011). After these five calibration steps, the echelle spectra were dark-subtracted, flat-fielded, and rectified, and the orders stitched (12, 15 and 16 for the UVB, VIS and NIR arms, respectively). The sky was then subtracted using adjacent exposures. Standard star observations were reduced with the same calibration data as the science frames and used to correct for telluric absorption and detector response. A final spectrum was created by mean stacking all exposures. We refer to Geier et al. (2013) for a detailed description of reduction steps of Xshooter spectra.

2.2.3. GTC-Osiris

The target was also observed using the Gran Telescopio Canarias (GTC) with the Osiris optical spectrograph (Cepa et al. 2003) in long-slit mode with the R1000B grism (dispersion of 2.12 \AA px^{-1}) and a 0.8 $''$ wide slit, resulting in a spectral resolution of $R \sim 800$. Observations were carried out in queue mode under clear sky conditions under programs GTC8-11B and GTC22-12B (PI: Fernández-Soto). During the 2011/2012 winter we obtained two separate runs. The first one was acceptable (average seeing of 0.9 $''$), but the second was below the expected quality and the data were not useful (seeing worse than 1.5 $''$). In each of them three exposures of 840 seconds each were taken, using offsets of +1.78 $''/0''/-1.78''$ along the slit. A third run in February 2013 obtained three more exposures of 900 seconds each, with an adequate seeing (1.0 $''$) and using the same observing strategy. In all cases the orientation of the slit was set to include a bright point source to serve as reference when analyzing and combining the two dimensional rectified frames.

Data reduction was performed using the standard long-slit package in IRAF (Valdes 1992), and all previous image calibration steps (bias subtraction, trimming, flat/fielding) before the final frame combination for each separate run were also performed within IRAF. Wavelength calibration was obtained using the HgAr and Ne arclamp exposures provided by the Observatory, and the images were rectified to correct obvious

¹⁰ IRAF is distributed by the National Optical Astronomy Observatory, which is operated by the Association of Universities for Research in Astronomy (AURA), Inc., under cooperative agreement with the National Science Foundation.

flexures along the spatial direction. An approximate flux calibration was obtained via the observations of the spectrophotometric standard stars G191-B2B or GD158-100.

2.2.4. Extraction of One-dimensional Spectra

Following Horne (1986), one-dimensional spectra were extracted by summing all adjacent lines (along the spatial direction) using weights corresponding to a Gaussian centered on the central row with a full width at half maximum (FWHM) equal to the slit width used in each observation. To correct for slit losses and obtain an absolute flux calibration, spectroscopic broad/medium-band fluxes were obtained by integrating over the corresponding filter curves, and a constant scaling was applied to each spectra individually. A binned, lower resolution spectrum with higher S/N was extracted for each spectra using optimal weighting, excluding parts of spectra contaminated by strong sky emission or strong atmospheric absorption. The resulting spectral resolutions of the binned Xshooter spectra were $R \approx 30-45$, $15-40$, and $20-50$ for the UVB, VIS, and NIR arms, respectively, while the spectral resolutions of the binned NIRSPEC spectra were $R \approx 30-100$ and $100-300$ for the H and K bands, respectively.

2.3. ACS-G800L Grism Spectrum

C1-23152 lies within the area observed with the *Hubble Space Telescope* (HST) ACS G800L grism by the 3D-HST survey (Brammer et al. 2012); unfortunately it lies outside of the area covered by the infrared G141 grism. The G800L grism covers the wavelength range $0.55-1.0 \mu\text{m}$ with a dispersion of $40 \text{ \AA pixel}^{-1}$ and a resolution of 80 \AA for point-like sources (Kummel et al. 2011). We extract a flux-calibrated spectrum for C1-23152 using the *aXe* software (Kummel et al. 2009). The G800L spectrum of C1-23152 has no significant contamination from overlapping spectra of nearby sources and has a total integration time of 3123 s.

2.4. ACS I_{814} and WFC3 H_{160} Imaging

C1-23152 has been observed with HST using the WFC3 and the F160W filter (H_{160} , hereafter) as part of the HST Cycle 20 program GO-12990 (PI: Muzzin). Four individual H_{160} exposures were aligned and combined with the *MultiDrizzle* software (Koekemoer et al. 2002) following the procedure outlined by Skelton et al. (2014). The combined H_{160} image has an exposure time of 861 s and is drizzled to a pixel scale of $0.''03 \text{ pixel}^{-1}$ with a point-source FWHM $\sim 0.''15$. ACS F814W (I_{814} , hereafter) imaging of C1-23152 is also available from the HST Cycle 12 program GO-9822 (Scoville et al. 2007).

3. ANALYSIS

3.1. Emission Features and Spectroscopic Redshift

The nebular emission lines that we set out to measure were $\text{Ly}\alpha$, $\text{CIV}\lambda 1549$, $\text{HeII}\lambda 1640$, $[\text{OII}]\lambda 3727$, $\text{H}\beta$ and $[\text{OIII}]\lambda\lambda 4959, 5007$. Upon visual inspection of the reduced two-dimensional spectra, the $\text{Ly}\alpha$ (both Xshooter and Osiris) and $[\text{OIII}]\lambda\lambda 4959, 5007$ lines were easily identified.

The emission lines (except $\text{Ly}\alpha$) were fit by a symmetric Gaussian profile plus a local continuum. In the case of the $[\text{OIII}]$ doublet (easily identifiable by eye), identical redshift and FWHM were assumed with the ratio of the amplitudes $[\text{OIII}]\lambda 4959/[\text{OIII}]\lambda 5007$ fixed to 1:3.

The $[\text{OII}]\lambda\lambda 3726, 3729$ line doublet in the H -band was fit as a single Gaussian emission line, based on signal-to-noise and spectral resolution considerations. The analysis of

$[\text{OII}]\lambda 3727$ and $\text{H}\beta$ lines was more complicated due to significant sky residuals at their locations. Therefore, their measurements were carried out in multiple approaches. First, we fit both lines with redshift and FWHM (velocity) fixed at the best-fit values obtained from $[\text{OIII}]$. We then left the width as a free parameter. The $\text{H}\beta$ spectral region was also modeled with two components, one in emission and the other in absorption, with the velocity (FWHM) and redshift of the emission component fixed at the $[\text{OIII}]$ values, but treated as free parameters for the absorption component. The $[\text{OII}]$ line is only marginally detected in emission and we obtained a 3σ upper limit for the $\text{H}\beta$ emission by assuming the amplitude of the emission line to be three times the uncertainty in the local continuum. CIV is detected in emission blue-shifted with respect to the redshift derived from $[\text{OIII}]$ (this is discussed later in this section). HeII is marginally detected with a possible signature of self-absorption (also seen for $\text{Ly}\alpha$; see below). We determined the redshift of the self-absorption component using the central wavelength of the best-fit Gaussian line profile in absorption on top of an emission component.

A Monte Carlo approach was used to measure the uncertainties in the centroid, flux, and width. For each spectra, 1000 simulated spectra were created by perturbing the flux at each wavelength of the true spectrum by a Gaussian random amount with the standard deviation set by the level of the 1σ error spectrum. Line measurements were obtained from the simulated spectra in the same manner as the actual data. We compute the formal lower and upper confidence limits by integrating the probability distribution of each parameter (centroid, width, continuum, and emission line flux) from the extremes until the integrated probability is equal to 0.1585.

The best fit values of the modeled spectral lines are listed in Table 2, with the quoted uncertainties corresponding to the 1σ errors estimated from the Monte Carlo simulations.

The profile of the $\text{Ly}\alpha$ emission is observed to be asymmetrically double-peaked in both the Xshooter and Osiris spectra, indicative of self-absorption, and we analyzed it with a number of approaches. We initially fit each peak independently with a Gaussian profile, assuming a constant continuum. Then, in order to account for the self-absorption, we fit the observed spectra simultaneously with two Gaussians, one in emission and the other in absorption. Finally, we fit the wings of the $\text{Ly}\alpha$ emission with a single Gaussian after masking the self-absorbed region between the two peaks in order to obtain the line width of the emission line. We determine that the higher S/N Xshooter spectrum samples the wings of the $\text{Ly}\alpha$ emission line better, resulting in a FWHM of $\sim 923.0 \pm 79.3 \text{ km s}^{-1}$, comparable with the widths found in other high- z Type II QSOs (Norman et al. 2002; Alexandroff et al. 2013).

In Figure 1 we show the observed one-dimensional spectra around the regions of the considered spectral lines. The regions of the spectra significantly affected by sky lines (shown by gray filled areas) were excluded from the line profile modeling. The redshift of a galaxy's nebular lines (e.g., $[\text{OII}]\lambda 3727$, $\text{H}\beta$, $[\text{OIII}]\lambda\lambda 4959, 5007$) is expected to be nearly equal to the redshift of its stars, i.e., the gas responsible for the nebular emission should always lie close to hot stars. We therefore choose the redshift of the $[\text{OIII}]$ emission lines, $z_{\text{spec}} = 3.351^{+0.001}_{-0.002}$, to be the systemic redshift of the galaxy.

Due to the resonant nature of the transition in neutral hydrogen, the interpretation of the origin of the $\text{Ly}\alpha$ emission is non-trivial (Verhamme et al. 2006; Kulas et al. 2012). In Figure 2 we show the spectroscopic redshifts and correspond-

TABLE 2. SPECTRAL LINE PROPERTIES

Feature	λ_{lab} (Å)	λ_{obs} (Å)	σ_{obs} (Å)	σ_{inst} (Å)	σ_{int} (Å)	z	FWHM (km s ⁻¹)	EW_{obs} (Å)	L (10 ⁴² ergs s ⁻¹)
<i>Keck-NIRSPEC</i>									
OIII	4960.295	21578.9 ^{+3.91} _{-7.67}	25.1 ^{+6.66} _{-6.60}	6.02	24.4 ^{+6.66} _{-6.60}	3.351 ^{+0.001} _{-0.002}	798.0 ^{+218.0} _{-215.9}	37.9 ^{+7.3} _{-6.6}	5.5 ^{+5.0} _{-2.9}
OIII	5008.240	21792.0 ^{+3.91} _{-7.67}	25.1 ^{+6.66} _{-6.60}	6.02	24.4 ^{+6.66} _{-6.60}	3.351 ^{+0.001} _{-0.002}	790.2 ^{+215.9} _{-214.90}	113.8 ^{+21.9} _{-19.8}	16.5 ^{+15.1} _{-8.8}
OIII ^a	3727.80	16220.5	19.13	6.24	18.08	3.351	786.9	54.4 ^{+29.8} _{-23.4}	7.54 ^{+10.1} _{-4.17}
OIII ^b	3727.80	16220.5	39.8 ^{+29.9} _{-14.6}	6.24	39.3 ^{+34.0} _{-14.6}	3.351	1710.0 ^{+1299.4} _{-634.9}	124.9 ^{+60.6} _{-56.6}	16.1 ^{+27.4} _{-11.5}
H β^a	4862.68	21158.7	24.4	6.24	23.6	3.351	786.9	-14.7 ^{+13.9} _{-14.6}	≤ 0.88
H β^b	4862.68	21158.7	28.3 ^{+40.0} _{-24.3}	6.24	27.6 ^{+40.0} _{-24.27}	3.351	920.6 ^{+1334.3} _{-809.5}	-16.8 ^{+39.1} _{-41.3}	≤ 1.3
H β (Em.+Abs.):									
Emission	4862.68	21158.676	24.4	6.24	23.6	3.351	786.9	39.0 ^{+∞} _{-39.0}	...
Absorption	4862.68	21158.676	27.9 ^{+33.6} _{-14.0}	6.24	27.2 ^{+33.6} _{-14.0}	3.351	907.0 ^{+1121.5} _{-467.3}	-74.7 ^{+51.1} _{-∞}	...
<i>VLT-Xshooter</i>									
Ly α	1215.24	5290.47 \pm 0.57	6.93 \pm 0.6	0.45	6.92 \pm 0.6	3.353 \pm 0.001	923.0 \pm 79.3	466.4 \pm 231.3	46.2 \pm 6.8
Ly $\alpha_{self-abs}$	1215.24	5290.58 ^{+1.53} _{-0.73}	3.354 ^{+0.001} _{-0.001}
Ly α_1	...	5284.6 ^{+0.70} _{-0.57}	1.75 ^{+0.76} _{-1.15}	0.45	1.69 ^{+0.76} _{-1.15}	3.349 ^{+0.001} _{-0.001}
Ly α_2	...	5293.6 ^{+1.40} _{-1.71}	8.01 ^{+2.46} _{-2.38}	0.45	8.00 ^{+2.46} _{-2.38}	3.356 ^{+0.001} _{-0.001}
HeII	1640.405	7132.4 ^{+3.64} _{-4.09}	5.49 ^{+3.52} _{-3.27}	0.34	5.48 ^{+3.52} _{-3.27}	3.348 ^{+0.003} _{-0.002}	542.1 ^{+249.5} _{-323.4}	48.3 ^{+22.8} _{-26.8}	8.46 ^{+10.6} _{-8.0}
HeII _{self-abs}	1640.405	7132.5 ^{+3.64} _{-3.64}	3.348 ^{+0.001} _{-0.001}
OIII	4960.295	21570.0 ^{+15.5} _{-8.10}	18.16 ^{+7.32} _{-9.82}	1.74	18.08 ^{+7.32} _{-9.82}	3.349 ^{+0.003} _{-0.002}	591.6 ^{+239.4} _{-239.4}	80.1 ^{+17.7} _{-36.4}	15.0 ^{+5.8} _{-1.4}
OIII	5008.240	21778.5 ^{+15.5} _{-8.10}	18.16 ^{+7.32} _{-9.82}	1.74	18.08 ^{+7.32} _{-9.82}	3.349 ^{+0.003} _{-0.002}	585.9 ^{+237.3} _{-318.3}	240.2 ^{+53.1} _{-109.0}	45.0 ^{+17.0} _{-4.3}
<i>GTC-Osiris</i>									
Ly α	1215.24	5289.1380 \pm 0.31	5.32 \pm 0.32	3.47	4.03 \pm 0.32	3.352 \pm 0.001	538.4 \pm 42.1	485.0 \pm 145.0	34.3 \pm 2.7
Ly $\alpha_{self-abs}$	1215.24	5288.3 ^{+0.6} _{-0.7}	3.352 ^{+0.001} _{-0.001}
Ly α_1	...	5283.1 ^{+0.5} _{-0.6}	2.57 ^{+0.99} _{-0.84}	3.47	...	3.347 ^{+0.001} _{-0.001}
Ly α_2	...	5293.9 ^{+0.6} _{-0.6}	2.94 ^{+0.68} _{-0.53}	3.47	...	3.356 ^{+0.001} _{-0.001}
CIV	1549.48	6732.6 ^{+2.3} _{-1.9}	6.83 ^{+1.30} _{-2.06}	4.35	5.26 ^{+1.30} _{-2.06}	3.345 ^{+0.002} _{-0.001}	551.3 ^{+136.3} _{-170.9}	36.5 ^{+25.0} _{-2.1}	3.35 ^{+3.11} _{-0.67}
CIV _{abs}	1549.48	6706.1 \pm 1.9	6.2 \pm 2.4	4.35	4.42 \pm 2.4	3.328 \pm 0.001	501.0 \pm 271.6	-17.1 ^{+1.6} _{-19.8}	...

NOTE. — λ_{lab} is the laboratory rest-frame wavelength of the targeted spectral lines; λ_{obs} is the observed wavelength of the corresponding lines; σ_{obs} is the observed width of the modeled spectral lines; σ_{inst} is the instrumental width determined from the sky lines; σ_{int} is the intrinsic width of the spectral lines in the observed frame; z is the derived redshift; FWHM is the intrinsic velocity width of the spectral lines; EW_{obs} is the observed equivalent widths of the spectral lines; and L is the integrated line luminosity calculated using the adopted systemic redshift $z_{spec} = 3.351$. Listed errors correspond to the 1σ uncertainties derived from the Monte Carlo simulations. ^a denotes fits to emission lines with redshift and line width fixed to that of [OIII]; ^b denotes fits to emission lines with only the redshift fixed to that of [OIII].

ing uncertainties for all observed spectral lines. We note that the prominent double peaked Ly α in both the Xshooter and Osiris spectra brackets the systemic redshift of the galaxy, and the redshifts of the self-absorbing material obtained from both the Ly α and HeII are also consistent with the systemic redshift derived from [OIII].

We marginally detect an emission line with a potential P-Cygni profile at 6732Å in the Osiris spectrum, which we interpret as CIV λ 1549 emission blueshifted with respect to the systemic redshift by 425 km s⁻¹. P-Cygni line profiles are powerful diagnostics of outflow kinematics (Spoon et al. 2013). We fit the observed P-Cygni profile of CIV with a component in emission and a blue-shifted broad component in absorption. The absorption feature of the P-Cygni profile results blue-shifted by $\sim 1160 \pm 130$ km s⁻¹ with respect to the emission component. We note that high-ionization emission lines blue-shifted with respect to low-ionization emission lines have been previously observed in (particularly radio-quiet) luminous quasars (Richards et al. 2011), who argue that the apparent blueshift with respect to the systemic redshift might be the result of preferential reduction/obscuration of the red wing of the CIV emission line. We however stress that the CIV detection in the Osiris spectrum is marginally significant, and that CIV emission is not detected in the Xshooter spectrum, therefore caution is required when interpreting the

ambiguous CIV detection. Although a CIV emission feature is often used as evidence for the identification of active galactic nuclei (AGNs; Daddi et al. 2004, Hainline et al. 2011), it has been found to be missing in $z \sim 2.5$ AGNs with moderately broad (FWHM ~ 1430 km s⁻¹) Ly α emission (Hall et al. 2004).

We calculated the fluxes of the observed emission lines by integrating the fitted Gaussian profiles, with uncertainties determined using the 1σ standard deviations derived from Monte Carlo simulations of the amplitude and velocity width of the fits. The line luminosities estimated using the adopted systemic redshift are listed in Table 2, which also lists the line velocities (FWHM) corrected for the instrumental profile (determined from the width of the sky lines). The [OIII] line width is $FWHM_{[OIII]} \approx 790 \pm 220$ km s⁻¹, in good agreement with the line widths observed in low-redshift Seyfert II galaxies (FWHM < 1200 km s⁻¹; Hao et al. 2005). The Ly α line width is slightly broader, with $FWHM_{Ly\alpha} \approx 920 \pm 80$ km s⁻¹.

3.2. SED Modeling and Stellar Population Properties

In this section we present the modeling of the observed SED of C1-23152 obtained by combining the photometry from NMBS and the spectra from the UV to the NIR, and we present the derived properties of its stellar population.

In order to robustly constrain the stellar population parameters, all spectra and photometry must be corrected for contam-

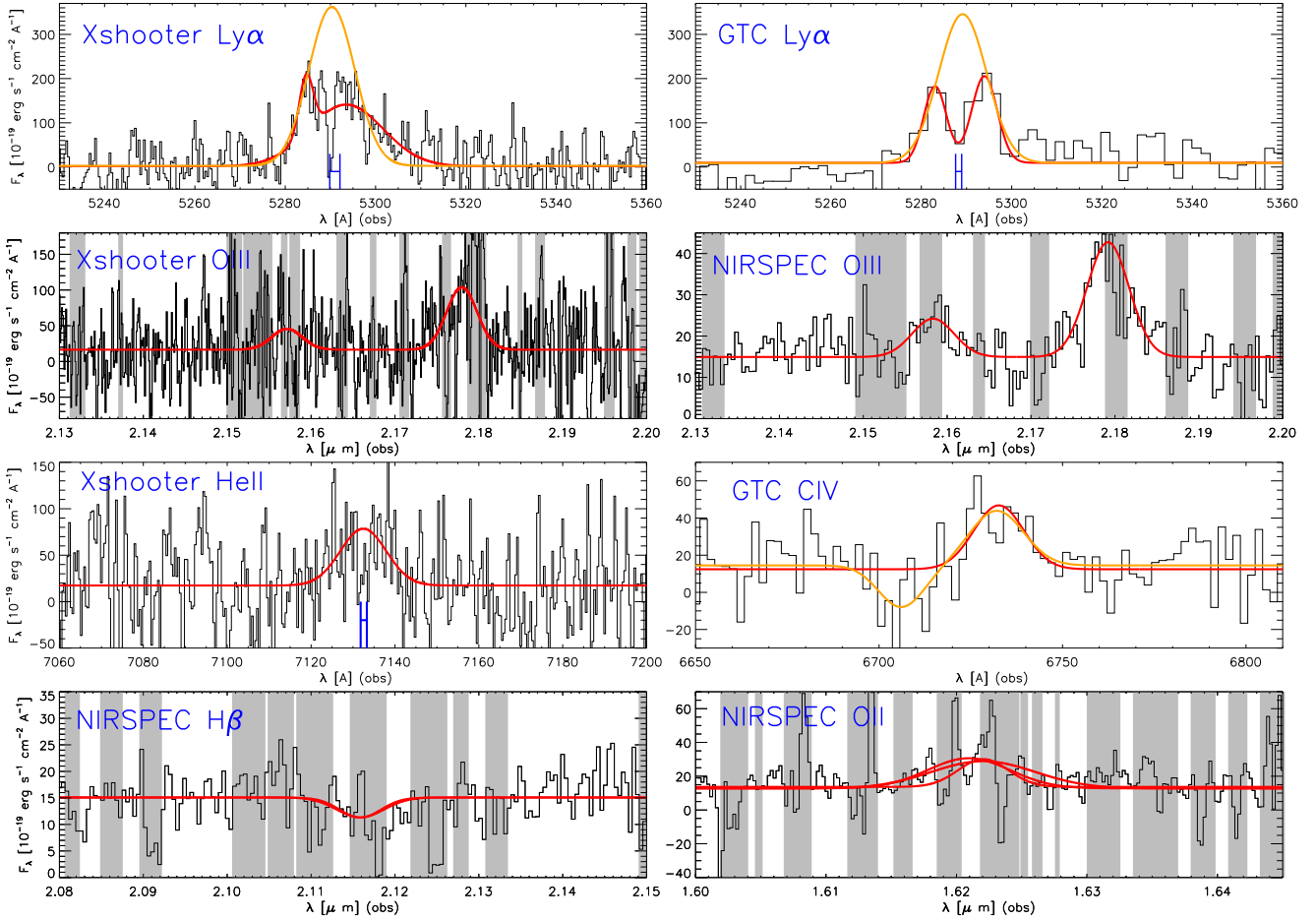


FIG. 1.— Observed one-dimensional spectra in the region around the considered spectral features. The red solid curves represent the best-fit Gaussian profiles to the emission lines. The orange solid curves in the top panels represent the best-fit single Gaussian profile after masking the self-absorbed region between the two $\text{Ly}\alpha$ peaks. The orange solid curve in the CIV panel represents best-fit P-Cygni profile. The gray shaded regions indicate regions of the spectra significantly affected by telluric sky lines. The best fit central wavelength and 1σ uncertainty of the central wavelength of the self-absorption component of $\text{Ly}\alpha$ and HeII is indicated by the blue brackets in the corresponding panels.

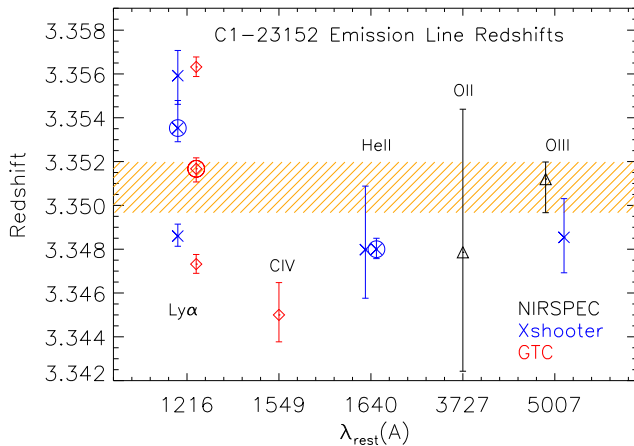


FIG. 2.— Spectroscopic redshifts obtained from different emission lines. *Blue crosses* show the redshifts of spectral features measured in the Xshooter spectra; *red diamonds* show the redshifts of spectral features measured in the Osiris spectra; *black triangles* indicate the redshifts of spectral features measured in the NIRSPEC spectra. Open circles represent the redshifts measured from the self-absorption features in the $\text{Ly}\alpha$ and HeII lines. The orange hatched region indicates the adopted systemic redshift for C1-23152 based on the higher S/N NIRSPEC [OIII] detection, i.e., $z_{\text{spec}} = 3.351^{+0.001}_{-0.002}$.

ination from nebular emission lines. We determined the necessary emission-line corrections for all observed photometries by comparing the observed-frame equivalent width of each emission line to the bandwidth of corresponding filter. We found that the contributions due to [OII] and [OIII] amount to $< 5\%$ in the NMBS H_1 , H , K , and K_S bands. The contributions due to $\text{Ly}\alpha$ emission were much more significant in the g and V broad-bands, $\sim 60\%$ and $\sim 90\%$, respectively. We also removed the photometry belonging to the medium-band IA527 (Subaru) from the fitting routine as this band was completely dominated by the $\text{Ly}\alpha$ emission.

We estimated the stellar population properties by fitting the binned, low-resolution UVB, visual, and NIR Xshooter, NIRSPEC, and ACS grism spectra in combination with the broad-band and medium-band photometry with stellar population synthesis (SPS) models. We excluded the Osiris spectrum due to its lower S/N compared to the binned Xshooter spectrum and the photometry in the same wavelength regime. We used FAST (Fitting and Assessment of Synthetic Templates; Kriek et al. 2009) to model and fit a full grid in metallicity, dust content, age, and star formation timescale. We investigated different star formation histories (SFH), i.e., the exponentially declining, the delayed-exponentially declining, and the truncated SFHs. We adopted stellar population synthe-

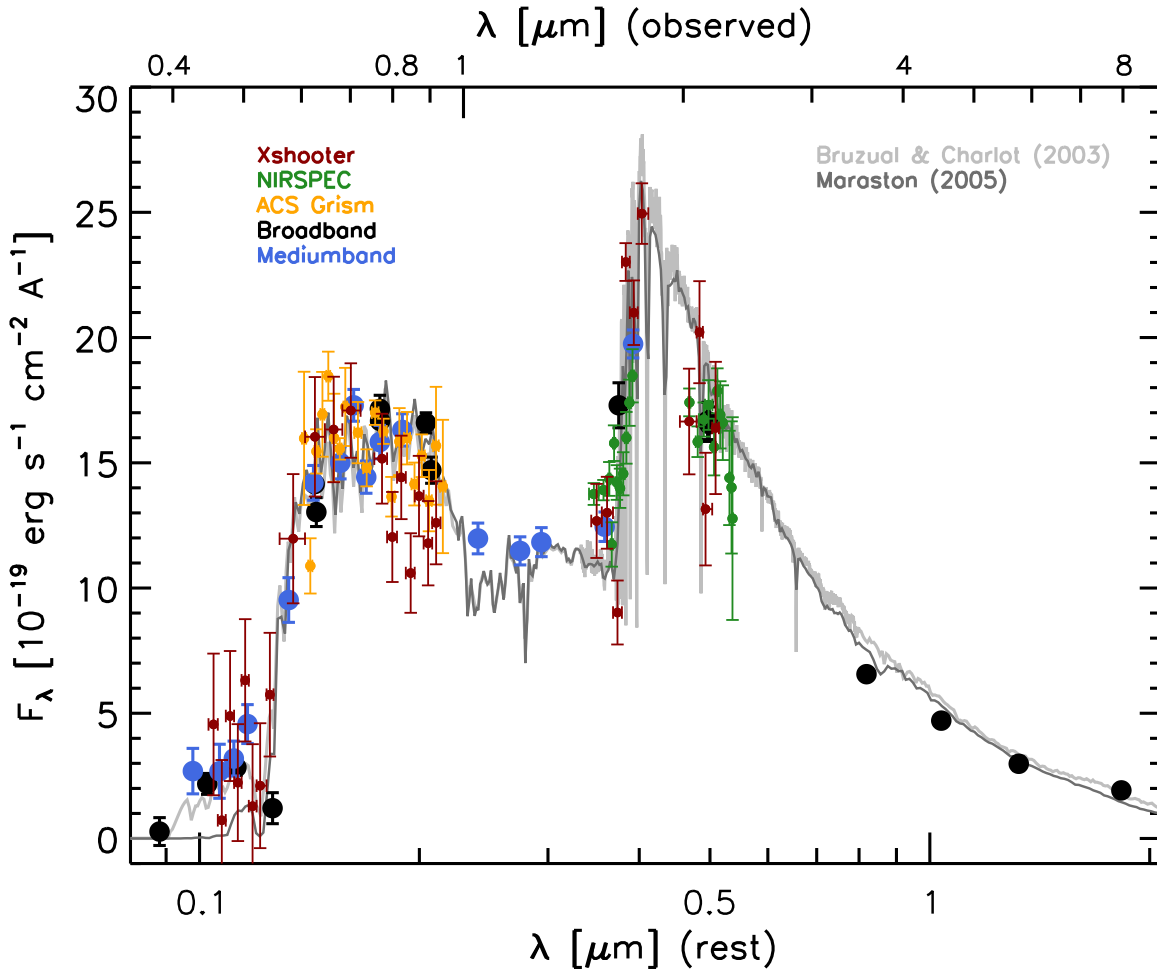


FIG. 3.— Observed SED from the combination of the medium- (blue filled circles) and broad-band (black filled circles) NMBS photometry and the binned spectra (NIRSPEC in green; ACS grism in orange; and Xshooter in maroon) redshifted to the rest frame. The light and dark gray curves represent the best-fit models adopting the BC03 and MA05 stellar population models, respectively, with an exponentially declining SFH and free metallicity.

sis models from both Bruzual & Charlot (2003) and Maraston (2005) (BC03 and MA05, hereafter), and we assumed the Kroupa (2001) IMF and the Calzetti et al. (2000) extinction law. The age range allowed was between 10 Myr and 3.16 Gyr (the maximum age of the universe at the redshift of the galaxy) with a step size of 0.1 dex. We adopted a grid for τ between 3.16 Myr and 10 Gyr in steps of 0.10 dex. We allowed the dust attenuation (A_V) to range from 0 to 3 mag with step size of 0.01 mag. Metallicity can vary between $Z = 0.004, 0.08, 0.02, 0.05$ or $Z = 0.001, 0.01, 0.02, 0.04$ for the BC03 and the MA05 templates, respectively. We initially modeled the observed SED with the metallicity as a free parameter and then we repeated the modeling by treating the metallicity as a systematic uncertainty by fixing it at the available values.

Figure 3 shows the observed SED blueshifted to the rest-frame of the galaxy with the MA05 and BC03 stellar population synthesis models and an exponentially declining SFH. The results of the SED-modeling and the corresponding 3σ errors are listed in Table 3.

As shown by the values in Table 3, the median stellar mass derived adopting the BC03 models is $\log(M_*/M_\odot) = 11.49 \pm 0.08$. The error budget is dominated by the systematic uncertainties due to different SED-modeling assumptions. Nonetheless, given the very high-quality and sampling

of the SED of C1-23152, different modeling assumptions affect the derived stellar mass by at most ± 0.08 dex, i.e., $< 20\%$. Independently of the SED-modeling assumptions, the best-fit dust attenuation is zero, with a 3σ upper limit of ~ 0.4 mag when the observed SED is modeled with MA05 stellar population synthesis models, a delayed-exponentially declining SFH, and super-solar metallicity. This combination of SED-modeling assumptions also results in the largest 3σ upper limit for the SFR, i.e., $7 M_\odot \text{ yr}^{-1}$. However, most of the other combinations of SED-modeling assumptions result in low or negligible SFRs, with a more typical 3σ upper limit of $2\text{--}5 M_\odot \text{ yr}^{-1}$. The best-fit SFR-weighted mean stellar age ($\langle t \rangle_{\text{SFR}}$ of the galaxy (as defined in Förster Schreiber et al. 2004) is 350 Myr when adopting BC03 models and a best-fit solar metallicity, and a factor of 2 smaller when adopting MA05 models with a best-fit super-solar metallicity. We note that the stellar age can vary by as much as ± 0.2 dex depending on the metallicity. The preferred timescale of the duration of the burst (τ) is always very short, < 70 Myr at 3σ , with a typical best-fit value of ~ 50 Myr. We finally note that the value of τ is found to be systematically lower by as much as a factor of ~ 8 when the MA05 models are assumed. The best-fit stellar age of ~ 400 Myr implies a formation redshift of $z_{\text{form}} \sim 4.1$.

Compared to the stellar population parameters derived in

Marchesini et al. (2010) for C1-23152 based only on the NMBS photometry, we find that the stellar mass is larger by ~ 0.07 dex, SFR larger by ~ 1.5 dex (but well within the quoted uncertainties listed in Marchesini et al. 2010) and the stellar age older by ~ 0.5 dex.

3.3. Star Formation Rate from [OII]

We used the emission line [OII] $\lambda 3727$ as an independent measure of the SFR and compared it to the values obtained from SED fitting. We obtained a first order upper limit by assuming there is no AGN contribution to the [OII] emission line, and used the [OII] line luminosity-SFR relation defined in Kennicutt (1998), adapted for a Kroupa (2001) IMF.

We obtained $\text{SFR}([\text{OII}]) = 67 \pm 35 M_{\odot} \text{ yr}^{-1}$ (1σ error), larger by a factor of ~ 20 (for an exponentially-declining SFH) and ~ 140 (for a delayed exponentially-declining SFH) compared to the best-fit SFR values from the SED modeling. Assuming the [OIII] line is purely of AGN origin in our spectra, we adopted an empirical relation between [OII] and [OIII] to remove the component of the detected [OII] line that can be attributed to the presence of an AGN. Silverman et al. (2009) used the ratio [OII]/[OIII]=0.21 found in type 1 AGN in the SDSS sample with $\log L_{[\text{OIII}]} > 41.5$ to provide an estimate of the [OII] emission line luminosity free of any AGN contribution. We used this value to calculate an AGN-corrected upper limit to the SFR of the galaxy based on [OII] emission line luminosity. We obtained $\text{SFR}([\text{OII}]_{\text{AGNcorrected}}) = 36^{+40}_{-34} M_{\odot} \text{ yr}^{-1}$, marginally consistent within the errors with the SFR derived from SED modeling. However, we note that the [OII]-derived SFR is very uncertain due to the large uncertainties in the [OII] line flux measurements caused by the significant sky-line contamination in the spectral region where the redshifted [OII] line falls.

3.4. Emission Line Properties: AGN vs. Star Formation?

One diagnostic of AGN in several studies has been the luminosity of the [OIII] $\lambda 5007$ optical nebular emission. We confirm that C1-23152's [OIII] emission is indeed very luminous, $L_{[\text{OIII}]} = 1.65 \times 10^{43} \text{ erg s}^{-1}$, satisfying AGN selection criterion. This value is at the high end of the range of [OIII] luminosities found for Lyman Break galaxies (LBG) and Ly α emitters (LAE) at $z \simeq 2-4$ (Teplitz et al. 2000; Pettini et al. 2001; Maschietto et al. 2008; Kuiper et al. 2011; McLinden et al. 2011), and well above the threshold of $L_{[\text{OIII}]} > 10^{41.7} \text{ erg s}^{-1}$ for luminous Type-2 AGN classification (Mullaney et al. 2013).

At $z \gtrsim 3.3$, both [NII] $\lambda 6584$ and H α fall redward of the K-band, i.e., at wavelengths where spectroscopy is not yet feasible. In the absence of both these nebular emission lines, it is not possible to compare the line ratios of the galaxy on the most widely used emission line diagnostic, the BPT diagram (Baldwin, Phillips & Terlevich 1981), which employs optical nebular line ratios of [NII]/H α and [OIII]/H β to distinguish star-forming galaxies, Seyfert 2 galaxies (or AGN NLRs) and low-ionization nuclear emission-line region (LINER) galaxies.

Recently, Juneau et al. (2011, 2014) introduced a new excitation diagnostic that could be used in the absence of [NII] and H α measurements, namely the Mass-Excitation diagnostic (MEx). This diagnostic uses the well-known correlation between galaxy stellar mass and gas phase metallicity (Tremonti et al. 2004) to create an alternate BPT-like diagram with [OIII]/H β vs. stellar mass. We determine a lower limit to [OIII]/H β ratio by assuming that H β has the same

width as [OIII] and a peak flux three times the rms measured in the same spectral region, implying $\log([\text{OIII}]/\text{H}\beta) \geq 1.27$. Given the stellar mass derived from SED modeling, i.e., $\log(M_*/M_{\odot}) = 11.49$, the estimated lower limit on $\log([\text{OIII}]/\text{H}\beta)$ implies the presence of an AGN in C1-23152, based on its position on the MEx diagnostic diagram. We also note that the estimated lower limit on $\log([\text{OIII}]/\text{H}\beta)$ is a factor of ~ 4 larger compared to the unusually high mean [OIII]/H β ratio found by Holden et al. (2014) in a sample LBGs at $z \sim 3.5$ with $\log(M_*/M_{\odot}) < 10.5$ and significantly larger specific SFR (e.g., $\log(\text{sSFR}/\text{yr}^{-1}) > -9$) compared to C1-23152.

The large values for the line ratio of [OIII]/H β are inconsistent with stellar photoionization, and indicative of photoionization by an AGN. The AGN-interpretation is further confirmed by the comparably weak [OII] emission, such that the [OIII]/[OII] ratio $\sim 2.2^{+3.6}_{-1.7}$ (measured assuming identical widths and redshift for both lines). This line ratio is a sensitive diagnostic of the ionization parameter, and efficiently separates Seyfert-like objects from star-forming galaxies and LINERS at low redshift (Kewley et al. 2006). Because we lack any constraints on [OI]/H α that could further help separating the AGN from star-forming and composite galaxies, at [OIII]/[OII] >1 the main ambiguity is between Seyferts and low metallicity galaxies with significant ongoing star formation (Dopita et al. 2006; Nakajima et al. 2013). The upper limit on SFR obtained from [OII] line luminosity along with the small values of SFRs from the SED modeling provides strong evidence that the galaxy is not a star-bursting galaxy. The evaluation of C1-23152 using the MEx diagnostic further supports the AGN-like nature of the line emissions.

3.5. Continuum Emission from the AGN

In the previous sections, we found that C1-23152 likely hosts a luminous AGN from emission line properties. The AGN continuum emission could potentially contribute to the observed SED, biasing the derived stellar population parameters. We investigated this by subtracting the AGN contribution from the observed SED and by re-fitting the corrected SED. Specifically, we assumed a power-law SED for the AGN, with $F_{\nu} \propto \nu^{\alpha}$. The value of α was derived by fitting the rest-frame UV and the MIPS $24\mu\text{m}$ photometry and spectroscopy for maximal AGN SED contribution, corresponding to $\alpha \sim -1.6$. The maximum AGN contribution is then set by the rest-frame UV fluxes in combination with the $24\mu\text{m}$ band, and subtracted from the observed SED. The resulting SED is finally re-modeled using FAST to derive stellar population parameters (listed in Table 3). We find that the derived stellar mass is smaller by ~ 0.05 dex, resulting in $\log(M_*/M_{\odot}) = 11.44$ (i.e., $M_* \approx 2.8 \times 10^{11} M_{\odot}$).

We also used QSO templates from Polletta et al. (2007) to fit the maximum AGN continuum contribution in a similar manner as above to constrain the stellar population parameters of the galaxy. The templates used include the heavily obscured broad absorption line (BAL) QSO, Mrk231, and optically selected QSO with different IR to optical flux ratios. The AGN-continuum subtracted SED's were re-modeled using FAST with a Kroupa IMF, exponentially declining SFH and BC03 stellar population synthesis models, and the best-fit stellar properties are listed in Table 3. Figure 4 shows the observed SED of C1-23152 from the U-band to the MIPS $24\mu\text{m}$ overplotted on the adopted AGN templates with their maximum contributions constrained by the observed SED. Also plotted are the combinations of the best-fit FAST models of

TABLE 3. BEST FIT STELLAR POPULATION PARAMETERS

	$\log(\tau)$ (yr)	Metallicity	$\log(\text{Age})$ (yr)	A_V (mag)	$\log(M_*)$ (M_\odot)	SFR ($M_\odot \text{ yr}^{-1}$)	sSFR $\log(\text{yr}^{-1})$	χ^2
<i>SFH: Exponentially declining</i>								
Free Z	$7.70^{+0.02}_{-0.30}$	$0.02^{+0.030}_{-0.003}$	$8.60^{+0.02}_{-0.23}$	$0.00^{+0.14}_{-0.00}$	$11.49^{+0.00}_{-0.09}$	$2.88^{+1.01}_{-2.28}$	$-11.03^{+0.20}_{-0.58}$	3.56
Free Z	$(7.00^{+0.40}_{-0.23})$	$(0.04^{+0.000}_{-0.006})$	$(8.30^{+0.03}_{-0.06})$	$(0.0^{+0.2}_{-0.0})$	$(11.41^{+0.05}_{-0.03})$	$(0.00^{+5.13}_{-0.00})$	$(-15.40^{+4.66}_{-4.54})$	(3.89)
Z=0.004	$7.80^{+0.03}_{-1.30}$	0.004	$8.80^{+0.00}_{-0.10}$	$0.00^{+0.05}_{-0.00}$	$11.56^{+0.00}_{-0.05}$	$0.37^{+0.00}_{-0.37}$	$-11.90^{+0.00}_{-0.87}$	3.86
Z=0.008	$7.70^{+0.10}_{-1.20}$	0.008	$8.70^{+0.01}_{-0.12}$	$0.00^{+0.12}_{-0.00}$	$11.54^{+0.00}_{-0.07}$	$0.44^{+1.91}_{-0.44}$	$-11.90^{+0.78}_{-0.78}$	3.80
Z=0.02	$7.70^{+0.02}_{-0.64}$	0.02	$8.60^{+0.01}_{-0.10}$	$0.00^{+0.09}_{-0.00}$	$11.49^{+0.00}_{-0.06}$	$2.88^{+0.00}_{-2.88}$	$-11.03^{+0.00}_{-6.57}$	3.52
Z=0.05	$7.50^{+0.00}_{-0.10}$	0.05	$8.40^{+0.00}_{-0.03}$	$0.10^{+0.04}_{-0.10}$	$11.42^{+0.00}_{-0.02}$	$3.89^{+0.00}_{-3.29}$	$-10.83^{+0.00}_{-0.78}$	3.52
<i>SFH: Delayed exponentially declining</i>								
Free Z	$7.60^{+0.15}_{-1.10}$	$0.008^{+0.042}_{-0.004}$	$8.70^{+0.14}_{-0.33}$	$0.00^{+0.13}_{-0.00}$	$11.49^{+0.06}_{-0.08}$	$0.48^{+4.65}_{-0.48}$	$-11.81^{+1.09}_{-0.87}$	3.63
Free Z	$(6.70^{+0.70}_{-0.20})$	$(0.04^{+0.000}_{-0.015})$	$(8.30^{+0.10}_{-0.14})$	$(0.00^{+0.42}_{-0.00})$	$(11.41^{+0.11}_{-0.02})$	$(0.00^{+6.76}_{-0.00})$	$(-21.55^{+10.92}_{-8.78})$	(3.92)
Z=0.004	$7.60^{+0.05}_{-0.10}$	0.004	$8.80^{+0.02}_{-0.05}$	$0.00^{+0.03}_{-0.00}$	$11.55^{+0.00}_{-0.03}$	$0.03^{+0.00}_{-0.00}$	$-13.08^{+1.17}_{-0.00}$	3.63
Z=0.008	$7.60^{+0.20}_{-1.10}$	0.008	$8.70^{+0.10}_{-0.13}$	$0.00^{+0.16}_{-0.00}$	$11.49^{+0.07}_{-0.03}$	$0.48^{+3.07}_{-0.48}$	$-11.81^{+0.80}_{-0.87}$	3.59
Z=0.02	$7.50^{+0.10}_{-0.99}$	0.02	$8.60^{+0.02}_{-0.17}$	$0.00^{+0.18}_{-0.00}$	$11.48^{+0.00}_{-0.06}$	$0.58^{+4.10}_{-0.58}$	$-11.72^{+0.90}_{-25.02}$	3.71
Z=0.05	$7.30^{+0.20}_{-0.77}$	0.05	$8.40^{+0.10}_{-0.14}$	$0.10^{+0.22}_{-0.10}$	$11.41^{+0.03}_{-0.03}$	$0.51^{+3.75}_{-0.51}$	$-11.52^{+0.80}_{-13.89}$	3.76
<i>SFH: Truncated</i>								
Free Z	$8.20^{+0.43}_{-1.70}$	$0.008^{+0.042}_{-0.004}$	$8.70^{+0.23}_{-0.46}$	$0.00^{+0.33}_{-0.00}$	$11.50^{+0.08}_{-0.12}$	0	-99	3.62
	$(7.40^{+0.93}_{-0.90})$	$(0.04^{+0.000}_{-0.039})$	$(8.30^{+0.17}_{-1.30})$	$(0.00^{+2.50}_{-0.00})$	$(11.41^{+0.12}_{-0.04})$	(0)	(-99)	(4.54)
<i>AGN continuum subtracted; SFH: Exponentially declining</i>								
$\alpha \sim 1.6$								
Free Z	$7.70^{+0.82}_{-1.20}$	$0.02^{+0.03}_{-0.013}$	$8.60^{+0.14}_{-0.3}$	$0.00^{+0.10}_{-0.00}$	$11.44^{+0.14}_{-0.01}$	$2.57^{+0.00}_{-2.57}$	$-11.03^{+0.00}_{-99}$	4.43
<i>Mrk231 template</i>								
Free Z	$7.70^{+0.05}_{-1.20}$	$0.02^{+0.03}_{-0.009}$	$8.60^{+0.08}_{-0.34}$	$0.00^{+0.25}_{-0.00}$	$11.46^{+0.00}_{-0.14}$	$2.69^{+0.94}_{-0.00}$	$-11.03^{+0.20}_{-21.05}$	4.52
<i>DR2 template</i>								
Free Z	$7.50^{+0.10}_{-1.00}$	$0.02^{+0.03}_{-0.005}$	$8.60^{+0.04}_{-0.21}$	$0.00^{+0.07}_{-0.00}$	$11.49^{+0.01}_{-0.11}$	$0.05^{+0.41}_{-0.05}$	$-12.80^{+0.99}_{-25.70}$	8.03
<i>TQSO1 template</i>								
Free Z	$6.90^{+0.73}_{-0.40}$	$0.05^{+0.00}_{-0.038}$	$8.40^{+0.27}_{-0.04}$	$0.00^{+0.02}_{-0.00}$	$11.39^{+0.11}_{-0.01}$	$0.00^{+0.46}_{-0.00}$	$-20.03^{+8.22}_{-18.47}$	7.91

NOTE. — Estimated stellar population parameters from the modeling of the binned UV-to-NIR spectra in combination with the broad- and medium-bandwidth photometry from NMBS. The values in parenthesis correspond to the best-fit stellar population parameters assuming the Maraston (2005) stellar population synthesis models, while the values not in parenthesis correspond to the best-fit parameters derived assuming the Bruzual & Charlot (2003) stellar population synthesis models. Quoted errors are 3σ confidence intervals output by FAST (see Kriek et al. 2009 for a detailed description of the adopted method in FAST to estimate confidence intervals). A Kroupa (2001) IMF and a Calzetti et al. (2000) extinction law is assumed in all cases.

the AGN-continuum subtracted SED and the adopted AGN templates. The best fit stellar population parameters are again consistent with zero dust attenuation and low SFR; the stellar mass of the galaxy is lower on average by ~ 0.05 dex, compared to best-fit values modeled using the observed SED. The minimum stellar mass allowed by the 3σ uncertainties is $\log(M_*/M_\odot) = 11.32$ (i.e., $M_* \approx 2.1 \times 10^{11} M_\odot$), confirming that the observed SED of the galaxy is dominated by the stellar light, rather than the AGN emission, and confirming the very large stellar mass of C1-23152.

3.6. Further Evidence for Hidden Luminous Quasar

3.6.1. AGN luminosity

The AGN-like line ratios and line widths suggest that C1-23152 hosts a luminous AGN. If we ignore the contribution from strong ionizing radiation fields due to star formation, we can use the [OIII] luminosity as a direct proxy for the bolometric luminosity of the quasar. We used the bolometric correction ($C_{[\text{OIII}]}$) for extinction corrected $L_{[\text{OIII}]}$ derived by Lamastra et al. (2009) $L_{\text{bol,AGN}} \approx 454 L_{[\text{OIII}]}$ for extinction-corrected [OIII] luminosities to find $L_{\text{bol}} = 7.5^{+5.9}_{-3.3} \times 10^{45} \text{ erg s}^{-1}$. The authors in this study use a sample of type-2 AGN in SDSS with reliable $L_{[\text{OIII}]}$ and X-ray luminosities

(L_X) to estimate $C_{[\text{OIII}]}$ combining the observed correlation between $L_{[\text{OIII}]}$ and L_X with the X-ray bolometric correction (Marconi et al. 2004). We also estimated the ionizing luminosity, L_{ion} , from the total luminosity in narrow lines, L_{NLR} . Using $L_{\text{NLR}} = 3(3L_{[\text{OIII}]} + 1.5L_{[\text{OIII}]})$ and $L_{\text{ion}} = L_{\text{NLR}} \times C^{-1}$ and adopting a covering factor of $C \sim 10^{-2}$ (Rawlings & Saunders 1991), we find $L_{\text{ion}} = 14.2^{+6.6}_{-4.5} \times 10^{45} \text{ erg s}^{-1}$. Both estimates imply the presence of a luminous hidden quasar.

3.6.2. Spitzer-MIPS 24 μm Data

The observed 24 μm band probes the rest-frame $\sim 5.5 \mu\text{m}$, corresponding to the spectral region of thermal emission from hot dust at the redshift of C1-23152. The source of the mid-infrared (MIR) emission was investigated by Marchesini et al. (2010). Assuming that all the luminosity at the observed 24 μm is associated with dust-enshrouded star formation, the resulting SFR was found to be $\sim 1260 M_\odot \text{ yr}^{-1}$. This value is from many hundreds to a couple of thousands times larger than the SFRs estimated from SED modeling, and a factor of ~ 40 larger than the SFR estimated using the AGN-corrected [OII] line luminosity. The inconsistency of the 24 μm -derived SFR, which assumes that the mid-infrared emission originates from dust-enshrouded star formation, compared to the SED-

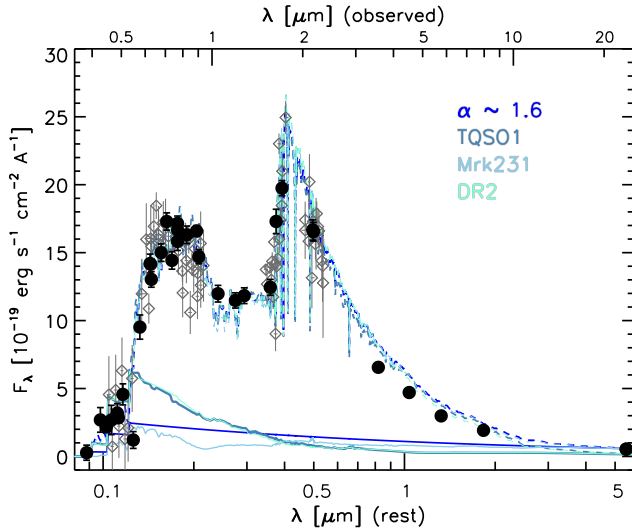


FIG. 4.— Observed SED of C1-23152 from the U -band to the MIPS $24\mu\text{m}$; filled black circles represent the broad- and medium-band photometry, while the gray open diamonds show the binned spectra. The continuous curves show the four AGN templates with their maximum contributions constrained by the observed $24\mu\text{m}$ flux and/or the rest-frame UV flux. The dashed curves show the combinations of the AGN templates and the best-fit FAST models obtained when fitting the AGN-continuum corrected SED of C1-23152. The different colors represent the four adopted AGN templates.

and [OII]-derived SFRs provides further evidence that C1-23152 hosts a powerful AGN, and that the dominant source of radiation responsible for heating the dust is the AGN.

To estimate the bolometric luminosity of the quasar independently of emission line luminosities, we used the two high- z composite templates of AGNs from Kirkpatrick et al. (2012), one with a clear $9.7\mu\text{m}$ silicate absorption feature and the other with a featureless MIR spectrum. We scaled the observed $24\mu\text{m}$ luminosity of C1-23152 to the rest-frame $5.5\mu\text{m}$ luminosity of the AGN templates. Using the integrated luminosities of the SED templates, we find $L_{\text{bol,AGN}} \approx (8.9 \pm 2.7) \times 10^{45} \text{ erg s}^{-1}$ and $L_{\text{bol,AGN}} \approx (15.2 \pm 6.5) \times 10^{45} \text{ erg s}^{-1}$ for the featureless AGN template and the AGN template with silicate absorption, respectively, in good agreement with the bolometric AGN luminosities estimated from the emission line luminosities.

3.6.3. Radio/X-ray Emission

We have used the publicly available Chandra X-ray data available over the COSMOS field (Elvis et al. 2009) to search for X-ray detection. C1-23152 is not detected. Using the 3σ detection flux limits, we derived the 3σ upper limit to the rest frame 2-10 keV luminosity of $L_{2-10\text{keV}} \approx 1.9 \times 10^{44} \text{ erg s}^{-1}$, assuming a power-law photon index of $\Gamma = 1.9$ (Nandra & Pounds 1994).

To investigate whether the expected X-ray flux of C1-23152 is below this detection limit, we used two methods to calculate the expected X-ray luminosity. We first employed the relation between mid-infrared ($12\mu\text{m}$) and X-ray luminosities observed by Gandhi et al. (2009) in local Seyferts, assuming the two high- z AGN SEDs as above. We found $L_{2-10\text{keV}} \approx 9.0 \pm 3.5 \times 10^{44} \text{ erg s}^{-1}$ and $\approx 9.1 \pm 3.6 \times 10^{44} \text{ erg s}^{-1}$ for the featureless and silicate AGN templates, respectively.

We also estimated the rest-frame $L_{2-10\text{keV}}$ luminosity using the bolometric correction adopted from Hopkins et al. (2007) again using the same two AGN SED templates as above.

The resulting X-ray luminosities are $L_{2-10\text{keV}} \approx 1.6 \pm 0.5 \times 10^{44} \text{ erg s}^{-1}$ and $\approx 2.4 \pm 1.1 \times 10^{44} \text{ erg s}^{-1}$ for the silicate absorption and the featureless templates, respectively. The estimated X-ray luminosities using the Gandhi et al. (2009) relation imply that the non-detection of C1-23152 in the X-rays would require a Compton-thick nature of the AGN, whereas the X-ray luminosities estimated using the bolometric correction from Hopkins et al. (2007) can be compatible with the observational flux limitations. We stress that these calibrations are based on low-redshift samples and the large uncertainties associated in both estimates prohibit us making firmer conclusions about the X-ray properties of C1-23152.

C1-23152 is also not detected in the publicly available 1.4 GHz VLA radio data available over the COSMOS field (Schinnerer et al. 2007). The sensitivity limit for the intrinsic $L_{1.4\text{GHz}}$ at the redshift of our target corresponds roughly to the classical boundary between radio-loud and radio-quiet AGN (i.e., $\log(L_{1.4\text{GHz}}[\text{W Hz}^{-1}])=25$; Schinnerer et al. 2007). Therefore, we are unable to make conclusive remarks on the radio properties of C1-23152. Given the numerous evidence for the (almost) post-starburst state of C1-23152, a non-detection is not surprising, as radio-loud AGNs are commonly found in hosts with $\text{SFR} \sim 300 \text{ M}_{\odot} \text{ yr}^{-1}$ at $z \sim 2$ (Floyd et al. 2013).

3.7. UVJ Colors

The rest-frame $U-V$ versus $V-J$ diagram (hereafter, UVJ diagram) has become a popular way to differentiate between star-forming and quiescent galaxies, with galaxy populations clearly separated in this color-color space (Labbé et al. 2005; Wuyts et al. 2007; Williams et al. 2009; Brammer et al. 2011; Whitaker et al. 2011; Patel et al. 2012, 2013; Muzzin et al. 2013b). Figure 5 shows the rest-frame $U-V$ and $V-J$ colors of C1-23152 (green) overplotted to the distribution in the UVJ diagram of all galaxies at $3.0 < z < 4.0$ from the K_S -selected UltraVISTA catalog of Muzzin et al. (2013a) (grayscale representation). We calculated the rest frame $U-V$ and $V-J$ colors of C1-23152 using EAZY (Brammer et al. 2008). A Monte Carlo approach was used to measure the uncertainties in the $U-V$ and $V-J$ colors. Specifically, 1000 photometry catalogs were created by perturbing each flux by a Gaussian random number with the standard deviation set by the level of each flux error. The simulated catalogs were each fit with EAZY separately, and the formal upper and lower limits were obtained in a similar manner as for the emission line fits.

The colors of C1-23152, $U-V = 0.89_{-0.02}^{+0.18} \text{ mag}$ and $V-J = 0.21_{-0.14}^{+0.06} \text{ mag}$, place it formally outside the commonly defined quiescent region, with a $U-V$ color intermediate between a star-forming galaxy with no dust and a quiescent post-starburst galaxy. Figure 5 also shows color-color evolution tracks for different SFHs and dust extinction. The gray and orange tracks represent the evolution of an exponentially declining SFH with $\tau = 100 \text{ Myr}$ and $A_V=0$ and 0.3 mag , respectively. The blue and light brown tracks represent the color evolution of constant star formation history with $A_V=0$ and 2.0 mag , respectively. Figure 5 shows that the derived $U-V$ and $V-J$ colors of C1-23152 match the colors predicted for a stellar population characterized by an exponentially declining SFH with $\tau = 100 \text{ Myr}$, no dust extinction, and an age of $\approx 0.5 \text{ Gyr}$, consistent within the errors with the stellar population properties of C1-23152 derived from the SED modeling.

3.8. Size

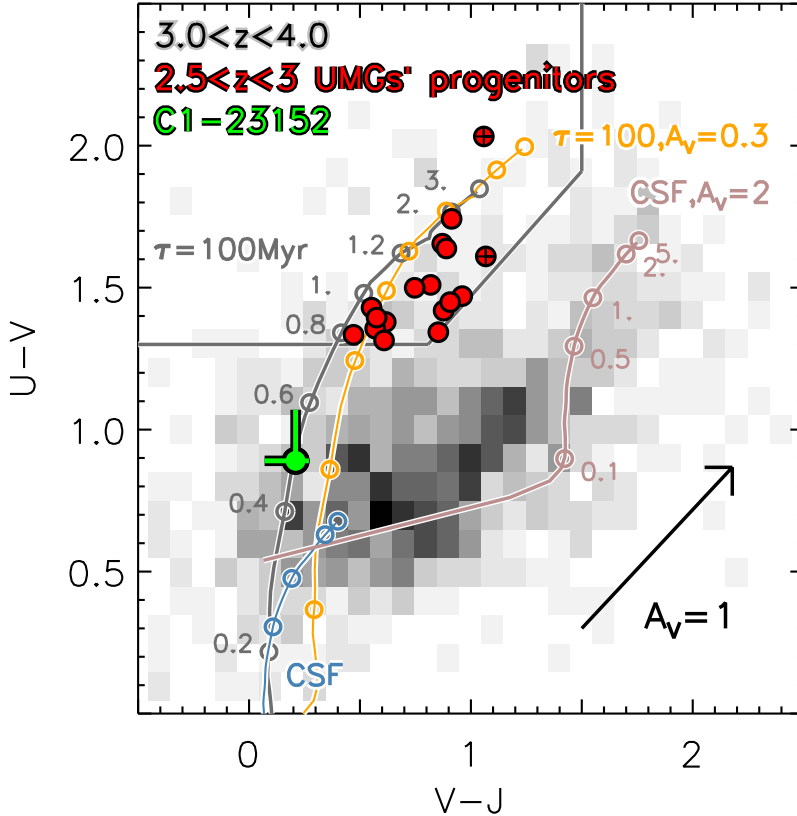


FIG. 5.— Rest frame $U-V$ versus $V-J$ color-color diagram. The *grayscale* representation indicates the distributions of galaxies at $3.0 \leq z \leq 4.0$ from the K_s -selected UltraVISTA catalog (Muzzin et al. 2013a). The cuts used to separate star-forming from quiescent galaxies from Muzzin et al. (2013b) are shown as the solid dark gray lines. The *green point* indicates the color for C1-23152, with error bars representing the total 1σ uncertainties. *Red filled points* are the quiescent progenitors of local UMGs at $2.5 < z < 3.0$ from Marchesini et al. (2014), with crosses indicating sources with MIPS detection at $\geq 5\sigma$. Color evolution tracks of Bruzual & Charlot (2003) models are also shown: an exponentially declining SFH with no dust ($\tau = 100$ Myr; gray), the same exponentially declining SFH with $A_V = 0.3$ mag ($\tau = 100$ Myr; orange), a constant SFH with no dust (CSF; light blue), and the same CSF model with $A_V = 2$ mag of extinction (light brown). The empty circles represent the model colors at the specified ages (in Gyr). The dust vector indicates an extinction of $A_V = 1$ mag for a Calzetti et al. (2000) extinction curve.

We used ACS I_{814} and *HST* F160W imaging to measure the structural parameters of the galaxy probing the rest frame UV ($\lambda_{\text{rest}} \approx 1870 \text{ \AA}$) and the rest-frame optical ($\lambda_{\text{rest}} \approx 3680 \text{ \AA}$), respectively. Structural parameters were obtained with GALFIT (Peng et al. 2002), which provides measurements of the Sérsic index (n), effective radius (r_e), and axis ratio (b/a). Visual inspection of the *HST* images showed that C1-23152 is accompanied by two fainter objects $\lesssim 2''$ south-west of its center. Although much fainter than C1-23152 (by ~ 2.5 and 3.6 mag in the H_{160} band, and ~ 2.6 mag in the I_{814} band), these two objects could contaminate the light profile of C1-23152, potentially introducing systematic effects in the recovery of the structural parameters. The measurements were therefore performed fitting the light profiles of the three sources simultaneously.

For each object, a single Sérsic profile was considered. The effective radius was circularized following the relation $r_{e,\text{circ}} = r_e \sqrt{b/a}$. The point spread function (PSF) in each *HST* band was built from a sample of bright and isolated point sources and combined together with the IRAF task `daophot/psf`. The PSF FWHM for the ACS I_{814} is $0.1''$ and $0.17''$ for the WFC3 H_{160} band. The values recovered for the circularized effective radius are $r_{e,\text{circ}} = 0.195'' \pm 0.021''$ and $r_{e,\text{circ}} = 0.130'' \pm 0.013''$ for the ACS I_{814} and the WFC3 H_{160} bands, respectively. The estimated values of the Sérsic

index and the axis ratios are $n = 5.5 \pm 0.5$ and $n = 4.4 \pm 0.4$, and $b/a = 0.85 \pm 0.04$ and $b/a = 0.82 \pm 0.03$ for the I_{814} and the H_{160} bands, respectively. Figure 6 shows, for each band, a cutout from the original frame centered on C1-23152, the GALFIT model, and the residual image after subtracting the model from the original frame. As a consistency check, we also run GALFIT masking the two neighboring sources and verifying that the morphological parameters obtained in this way did not differ sensibly from those obtained including the two neighboring sources. Figure 7 shows a color image obtained from the combination of the I_{814} and H_{160} bands of a cutout centered around C1-23152. Whereas C1-23152 shows a smooth and round morphology, with no obvious radial color gradient, the two nearby fainter sources are clearly bluer.

Observationally, an AGN could manifest itself as a brighter point source in the central region of the galaxy. Visual inspection of the residual images from the Sérsic profile fitting process did not show any evident sign of a residual point source. However, its existence was also tested by including a point-source component and re-running GALFIT. The resulting flux in each band was a value consistent with no flux, causing GALFIT to crash, and confirming the result from visual inspection. We finally re-run GALFIT by fixing the magnitude of the central point-source component to the values obtained from the maximized AGN contributions derived in §3.5. The contributions of the AGN to the total fluxes in the

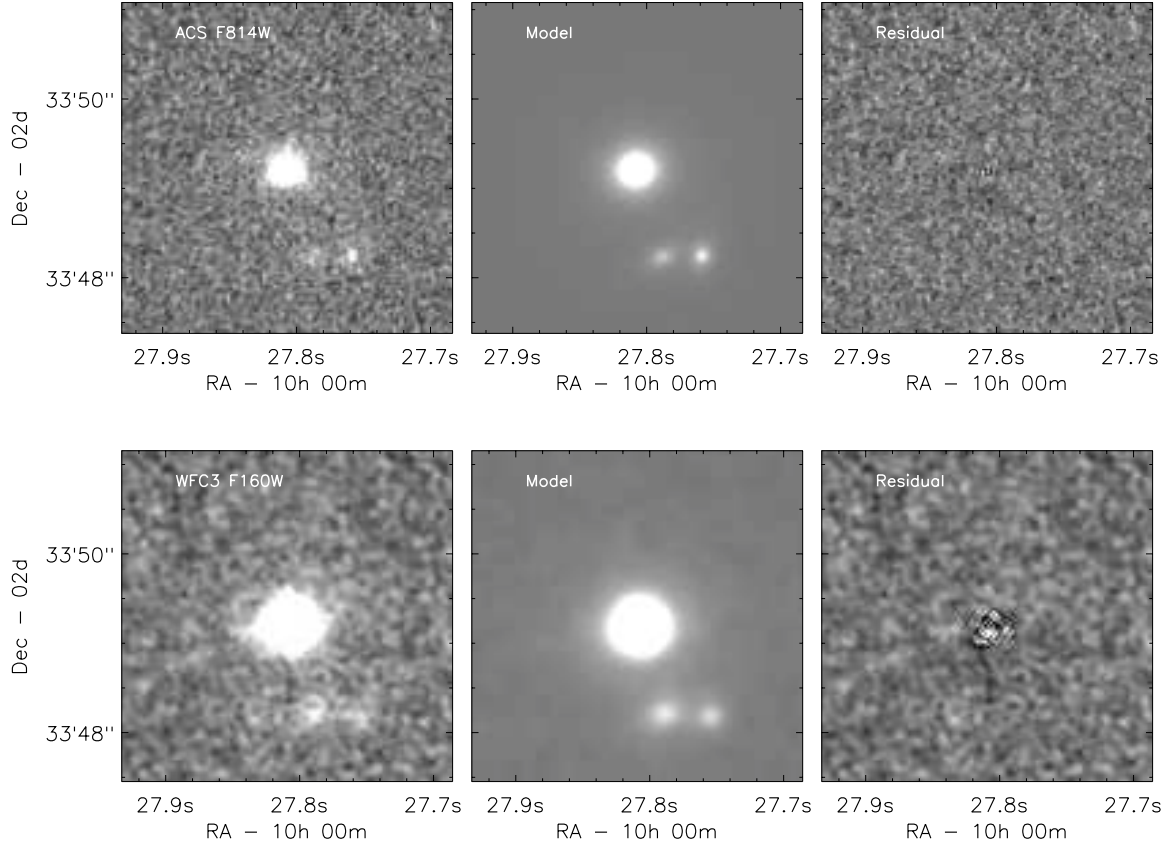


FIG. 6.— *Left Column:* ACS (top) and WFC3 (bottom) images for C1-23152. *Central column:* Best fit GALFIT modeling. *Right column:* Residual images.

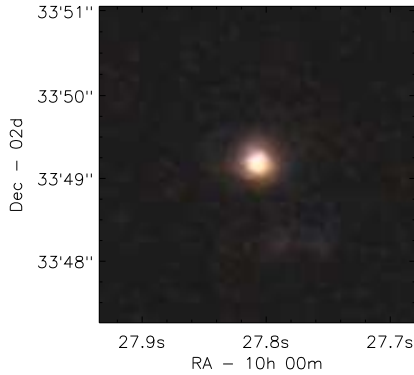


FIG. 7.— Color image obtained from the combination of the HST ACS I_{814} and WFC3 H_{160} bands centered around C1-23152. C1-23152 shows a smooth and round morphology; the two nearby fainter sources are characterized by bluer colors.

H_{160} and I_{814} bands is $\sim 8\text{--}15\%$ and $\sim 9\text{--}29\%$, respectively, depending on the AGN template. Fixing the magnitude of the central point-source component results in slightly larger effective radii, consistent within 2σ with the values obtained without a central point-source component. Specifically, we obtained $r_{e,\text{circ}} = 0.20''\text{--}0.23''$ and $r_{e,\text{circ}} = 0.14''\text{--}0.16''$ for the ACS I_{814} and the WFC3 H_{160} bands, respectively, depending on the adopted AGN contribution. Whereas the effective radius does not change significantly when including a central point-source, the Sérsic index is much more sensitive, and

ranges in $n = 0.7\text{--}3.9$ and $n = 3.0\text{--}3.6$ for the ACS I_{814} and the WFC3 H_{160} bands, respectively, depending on the adopted AGN contribution. We note however that the inclusion of the central point-source component results in increasingly worse modeling of the HST images for increasing AGN contributions, especially for the I_{814} band, and that significant positive and negative features appear in the center of the galaxy on the residual images output by GALFIT, indicative of over-subtraction of the central point-like component.

At the redshift of the source, $z_{\text{spec}} = 3.351$, the measured circularized effective radii correspond to linear sizes of $r_{e,\text{circ}} = 1.45 \pm 0.15$ kpc in the I_{814} and $r_{e,\text{circ}} = 0.97 \pm 0.1$ kpc in the H_{160} band.¹¹ Interestingly, the effective radius in the rest-frame UV is smaller than the effective radius in the rest-frame optical by $\sim 0.5 \pm 0.2$ kpc, with a gradient $\Delta \log r_{\text{eff}} / \Delta \log \lambda = -0.13 \pm 0.07$, broadly consistent with $\Delta \log r_{\text{eff}} / \Delta \log \lambda = -0.25$ in a sample of early-type galaxies at $0 < z < 2$ found by van der Wel et al. (2014). If we consider the circularized effective radius of ~ 1 kpc derived from the H_{160} band, C1-23152 is a very compact galaxy for its large stellar mass, arguably among the most compact very massive galaxies at $z > 3$. More quantitatively, the size of C1-23152 is a factor of ~ 2 smaller than the median size of galaxies at $2.5 < z < 3.0$ with similar stellar masses ($11 < \log M_*/M_\odot < 11.5$), and it is consistent with the 16% range in the size dis-

¹¹ When including a central point-source component with fixed magnitude constrained by the maximal contribution from the AGN continuum to the observed SED as derived in §3.5, the sizes increase to $r_{e,\text{circ}} = 1.49\text{--}1.73$ kpc in the I_{814} and $r_{e,\text{circ}} = 1.05\text{--}1.18$ kpc in the H_{160} band, consistent within 2σ with the sizes obtained without a central point-like component.

tribution of this sample (van der Wel et al. 2014). We finally note that C1-23152 is best modeled by a Sérsic index $n = 4.4 \pm 0.4$ in the H_{160} band, consistent with a de Vaucouleur’s profile ($n = 4$), and a large axis ratio of $b/a \sim 0.8 - 0.9$. The best-fit structural and stellar population parameters for C1-23152 are in line with other studies of early-type galaxies at $z > 1$ (Franx et al. 2008; van Dokkum et al. 2011; Wuyts et al. 2011; Wake et al. 2012; Bell et al. 2012; Chang et al. 2013) that have shown that sources with high Sérsic indices and large axis ratios are more likely to be quiescent.

4. SUMMARY AND DISCUSSION

In this paper we have investigated the extensive (observed-frame) UV-to-NIR spectra of a $z_{\text{phot}} \approx 3.3$, massive galaxy selected from the NMBS, namely C1-23152. We confirmed 1) the redshift of the source through the analysis of several nebular emission lines, and 2) the very large stellar mass of the galaxy by performing stellar population modeling of the spectral energy distribution of the galaxy corrected for both emission lines and AGN continuum. We also determined through analysis of emission line luminosities and line ratio diagnostics that C1-23152 likely hosts a luminous hidden AGN.

We found that C1-23152 is a very compact ($r_e \approx 1$ kpc), very massive ($\log(M_*/M_\odot) \gtrsim 11.3$) galaxy at $z_{\text{spec}} = 3.351$ with a formation redshift of $z \gtrsim 4$ with suppressed star formation, about to enter a post-starburst phase (as evidenced from the derived sSFR of $\log(\text{sSFR}/\text{yr}^{-1}) \sim -11$). We used both BC03 and MA05 stellar population models along with the Calzetti et al. (2000) extinction law and a Kroupa (2001) initial mass function with varying star formation histories to model the observed spectral energy distribution. We found that independently of SED-modeling assumptions, the best-fit attenuation is consistent with zero, the timescale of the burst (τ) is very short (~ 50 Myr) and the SFR is low (3σ upper limit is a $7 M_\odot \text{ yr}^{-1}$). The low SFR inferred from SED fits is inconsistent with the SFRs derived from both $L_{\text{[OIII]}}$ (and only marginally consistent when the [OII] luminosity is corrected for AGN contamination) and the observed MIPS $24\mu\text{m}$ flux if the $24\mu\text{m}$ detection is assumed to be due to dust-enshrouded star formation (by at least two orders of magnitude). The effect of different modeling assumptions change the derived stellar mass by at most ± 0.08 dex. However, the estimated stellar age ($\langle t \rangle_{\text{SFR}} \sim 350$ Myr when adopting the BC03 models and a best-fit solar metallicity) is much more sensitive to the different SED-modeling assumptions, with the stellar age a factor of ~ 2 smaller when adopting the MA05 models. We find strong evidence for the presence of a luminous hidden AGN ($L_{\text{bol,AGN}} \sim 10^{46} \text{ erg s}^{-1}$), potentially responsible for the quenching of the star formation. We employed the observed relation between MIR and X-ray luminosities and bolometric corrections using high- z AGN templates to estimate the rest-frame $L_{2-10\text{keV}}$ but cannot conclude with certainty whether the non-detection of C1-23152 in the X-ray is due to flux limitations of the data or a Compton-thick nature of the AGN.

Independent constraints on the mass of C1-23152 can be obtained from its kinematics. Using the velocity dispersion derived from the [OIII] line emission, we can attempt to estimate the dynamical mass of the galaxy using $M_{\text{dyn}} = C\sigma^2 r_e$, where C is a constant that depends on the structure of the galaxy and other parameters, and varies between $\log C = 5.87$ (the value resulting in $M_{\text{dyn}} \sim M_*$ for galaxies in the SDSS; Franx et al. 2008) and $\log C = 6.07$ (derived from kinematic data of local early-type galaxies; van Dokkum 2003). Using the measurements of the effective radius from the H_{160}

and the I_{814} bands, we estimated a dynamical mass ranging from $\log(M_{\text{dyn}}/M_*) = 10.91 \pm 0.24$ (adopting $\log C = 5.87$ and $r_e = 0.97$ kpc) to $\log(M_{\text{dyn}}/M_*) = 11.28 \pm 0.24$ (adopting $\log C = 6.07$ and $r_e = 1.45$ kpc), marginally consistent with stellar mass derived from the SED modeling. We note however that this calculation assumes that the [OIII] line is a reasonable probe of the overall gravitational potential of the galaxy. Whereas this assumption is plausible if the [OIII] emission originates from star formation and its line width is integrated over the entire galaxy, this does not appear to be the case for C1-23152, as the [OIII] emission appears to be mostly produced by the AGN narrow line regions. Velocity dispersion measurements from stellar absorption lines are therefore needed to robustly derive the dynamical mass of C1-23152.

Our findings for the properties of this galaxy fit well into the scenario for the formation of the progenitors of local giant elliptical galaxies proposed by Marchesini et al. (2014). Marchesini et al. (2014) studied the evolution of the properties of the progenitors of local UMGs in the last 11.4 Gyr since $z = 3$, finding that at $2.5 < z < 3.0$ a small fraction ($\sim 15\%$) of the progenitors are already quiescent, implying that the assembly of the very massive end of the local quiescent red-sequence population must have started at $z > 3$. The stellar population properties (i.e. stellar age, star formation rate, rest frame colors) of C1-23152 are qualitatively and quantitatively consistent with it being the progenitor of the already quiescent progenitors of local UMGs at $z = 2.75$, as clearly evident in Figure 5, which shows the relative position in the UVJ diagram of C1-23152 and the quiescent progenitors at $2.5 < z < 3.0$ of local UMGs from Marchesini et al. (2014) (red points in Figure 5). Furthermore, Figure 5 clearly shows that the difference in age between C1-23152 and the quiescent progenitors at $2.5 < z < 3.0$ of local UMGs is quantitatively consistent with the cosmic time between $z = 3.35$ and $z \approx 2.5 - 3$.

The large stellar surface densities observed in C1-23152 and other massive galaxies at $z = 2 - 3$ imply they must have formed via rapid, highly dissipative events at earlier times to account for the relatively small half-light radii and high Sérsic index n (Weinzirl et al. 2011). Although the exact physical picture underlying dissipative collapse mechanisms are uncertain (e.g., mergers, tidal interactions, Bounard et al. 2011; gas instabilities in turbulent diffuse disks, Ricciardelli et al. 2010), there is evidence that the radial gas inflows lead to centrally-concentrated starbursts (Mihos & Hernquist 1994; Ellison et al. 2010; Scudder et al. 2012), along with fueling the central super-massive black holes (SMBH). The subsequent energetic feedback from the active SMBH may be sufficient to regulate and quench star formation by preventing gas cooling (Kauffmann et al. 2000; Croton et al. 2006; Hopkins et al. 2008; van de Voort et al. 2011). Given the correlations between black hole mass, bulge mass, and n (Peng et al. 2006; Graham & Driver 2007; Gültekin et al. 2009), our findings that C1-23152 is a very massive and compact galaxy with high n undergoing a post-starburst phase with evidence for a hidden luminous quasar support this scenario. The relatively short lifetime of the quenching phase (Mendel et al. 2012) also justifies the low likelihood of observing galaxies in the same transitional phase as C1-23152.

Recently, Gilli et al. (2014) presented the study of an ultraluminous infrared galaxy at $z = 4.75$ in the Chandra Deep Field South, namely XID403. This source is found to be compact ($r \sim 0.9$ kpc), with a stellar mass estimated between $< 3 \times 10^{10} M_\odot$ (De Breuck et al. 2014) and $\sim 7 \times 10^{10} M_\odot$

(Gilli et al. 2014), depending on the amount of AGN contamination assumed in the rest-frame UV-to-NIR, and harboring a Compton-thick QSO. The SFR derived by fitting the far-IR SED is $\sim 650 M_{\odot} \text{yr}^{-1}$ (assuming Kroupa 2001 IMF), whereas fitting the optical/NIR SED results in $\text{SFR} \sim 180 M_{\odot} \text{yr}^{-1}$ (Gilli et al. 2014). The inferred stellar mass, size, gas depletion timescale ($\sim 10^7$ yr), and SFR of XID403 are consistent with it likely being the progenitor of the compact, quiescent, massive galaxies at $z < 3$. Our findings indicate that C1-23152 represents the transitioning phase between XID403 and the compact, massive, quiescent galaxies at $z < 3$. Its quenched star-formation activity while still harboring a hidden luminous AGN makes C1-23152 a natural descendent of XID403. With an intense burst of star formation in the recent past of C1-23152, one may expect a significant amount of dust in C1-23152 as produced by supernovae. The upper limits on the amount of dust obscuration resulting from the SED modeling ($A_V < 0.4$ mag) seems to imply that the mechanism responsible for the quenching of star formation in C1-23152 may also be responsible for the destruction of most of the dust produced in the intense starburst that produced the very large stellar mass of C1-23152.

Spectroscopic observations in both the optical and in the NIR of other candidates of very massive galaxies at $z > 3$ are of vital importance to confirm their redshifts, to better characterize the properties of their stellar populations, to distinguish between dust-enshrouded star formation and highly-obscured AGN activity, and to determine emission line and AGN contamination to the SEDs and mass-to-light ratios. High S/N rest-frame optical spectroscopy (especially redward of $\lambda_{\text{rest}} \sim 5000 \text{\AA}$) is needed to constrain star formation histories, SFRs, and metallicities, and to derive dynamical masses from stellar absorption lines for candidates of very massive galaxies in the first 2 Gyr of cosmic history (i.e., $z > 3$). NIR-Spec on the *James Webb Space Telescope* will provide the instrumental capabilities and sensitivities to successfully target stellar-mass complete samples of these candidates and to comprehensively understand the population of monster galaxies in the early universe. Observations with the *Atacama Large Millimeter Array* will also be crucial in discriminating between dust-enshrouded star-formation and obscured AGN activity as well as providing an independent estimate of the dynamical masses of the most massive galaxies through measurements of the kinematics in these systems. Finally, current X-ray data are inconclusive as to whether the non-detection of C1-23152 in the X-ray is due to observational flux limitations or a Compton-thick nature of the AGN hosted in C1-23152. In order to constrain the column density of X-ray absorbing matter, and hence whether the AGN is Compton-thick, observations in both soft and hard bands are necessary. *The Nuclear Spectroscopic Telescope Array Mission* (NuSTAR; Harrison et al. 2013) will provide an opportunity to attempt

addressing this issue.

ZCM gratefully acknowledges support from the John F. Burlingame and the Kathryn McCarthy Graduate Fellowships in Physics at Tufts University. DM and ZCM acknowledge the support of the Research Corporation for Science Advancement's Cottrell Scholarship, the support from Tufts University Mellon Research Fellowship in Arts and Sciences, and support from the programs HST-GO-12990 and HST-GO-12177.16, provided by NASA through a grant from the Space Telescope Science Institute, which is operated by the Association of Universities for Research in Astronomy, Incorporated, under the NASA contract NAS5-26555. MS acknowledges support from the programs HST-GO-12286.11 and 12060.95. AM acknowledges support from the Netherlands Foundation for Research (NWO) Spinoza grant. AFS acknowledges support from the Spanish Ministry for Science and Innovation and FEDER funds through grant AYA2010-22111-C03-02, and Generalitat Valenciana project Prometeo 2009/064. The Dark Cosmology Centre is funded by the Danish National Research Foundation. This study is partially based on data products from observations made with ESO Telescopes at the La Silla Paranal Observatory under programme ID 087.A-0514. Some of the data presented in this study were obtained at the W.M. Keck Observatory, which is operated as a scientific partnership among the California Institute of Technology, the University of California and the National Aeronautics and Space Administration. The Observatory was made possible by the generous financial support of the W.M. Keck Foundation. Keck telescope time was granted by NOAO, through the Telescope System Instrumentation Program (TSIP). TSIP is funded by NSF. The authors wish to recognize and acknowledge the very significant cultural role and reverence that the summit of Mauna Kea has always had within the indigenous Hawaiian community. We are most fortunate to have the opportunity to conduct observations from this mountain. Also based on observations made with the Gran Telescopio Canarias (GTC), installed in the Spanish Observatorio del Roque de los Muchachos of the Instituto de Astrofísica de Canarias, in the island of La Palma. This study makes use of data from the NEWFIRM Medium-Band Survey, a multi-wavelength survey conducted with the NEWFIRM instrument at the KPNO, supported in part by the NSF and NASA. We thank the NMBS and COSMOS collaborations for making their catalogs publicly available. This work is also partially based on observations taken by the 3D-HST Treasury Program (GO 12177 and 12328) with the NASA/ESA HST, which is operated by the Association of Universities for Research in Astronomy, Inc., under NASA contract NAS5-26555.

REFERENCES

- Alexandroff, R., Strauss, M. A., Greene, J. E., et al. 2013, MNRAS, 435, 3306
- Baldwin J. A., Phillips M. M., & Terlevich R. 1981, PASP, 93, 5
- Barro, G., Faber, S.M., Pérez-González, P.G., Pablo, G., ApJ, 765, 104
- Bell, E. F., van der Wel, A., Papovich, C., et al 2012, ApJ, 753, 167
- Bezanson, R., van Dokkum, P. G., Tal, T., et al. 2009, ApJ, 697, 1290
- Bournaud, F., Chapon, D., Teyssier, R., et al 2011, ApJ, 730, 4
- Brammer, G. B., van Dokkum, P. G., & Coppi, P. 2008, ApJ, 686, 1503
- Brammer, G. B., Whitaker, K. E., van Dokkum, P. G., et al. 2011, ApJ, 739, 24
- Brammer, G., van Dokkum, P. G., Franx, M., et al. 2012, ApJS, 200, 13
- Bruzual, G., & Charlot, S. 2003, MNRAS, 344, 1000
- Calzetti, D., Armus, L., Bohlin, R. C., et al. 2000, ApJ, 533, 682
- Capak, P., Aussel, H., Ajiki, M., et al. 2007, ApJS, 172, 99
- Cepa, J., Aguiar, M., Bland-Hawthorn, J., et al. 2003, in RMxAA Conference Series, Vol. 16, 13-18 (Eds. J. M. Rodríguez Espinosa, F. Garzon Lopez, & V. Melo Martin)
- Chang, Y. Y., van der Wel, A., Rix, H.-W., et al. 2013, ApJ, 773, 149
- Cimatti, A., Cassata, P., Pozzetti, L., et al. 2008, A&A, 482, 21
- Cowie, L. L., Songaila, A., & Hu, E. H. 1996, AJ, 112, 839
- Croton, D. J., Springer, V., White, S. D., et al. 2006, MNRAS, 365, 11
- Daddi, E., Cimatti, A., Renzini, A., et al. 2004, ApJ, 600, 127L

- Daddi, E., Renzini, A., Pirzkal, N., et al. 2005, *ApJ*, 626, 680
- De Breuck, C., et al. 2014, *A&A*, 565, A59
- D'Odorico, S., Dekker, H., Mazzoleni, R., et al. 2006, *Proc. SPIE*, 6269, 98
- Dopita, M. A., Firscher, J., & Sutherland, R. S. 2006, *ApJ*, 647, 244
- Ellison, S. L., Patton, D. R., Simard, L., et al. 2010, *MNRAS*, 407, 1514
- Elvis, M., et al. 2009, *ApJS*, 184, 158
- Floyd, D. J. E., Dunlop, J. S. D., Kukula, M. J., et al. 2013, *MNRAS*, 429, 2
- Föster Schreiber, N. M., van Dokkum, P. G., Franx, M., et al. 2004, *ApJ*, 616, 40
- Fontanot, F., De Lucia, G., Monaco, P., et al. (2009), *MNRAS*, 397, 1776
- Franx, M., van Dokkum, P. G., Schreiber, N.M., et al. (2008), *ApJ*, 688, 770
- Charlot, S., Brinchmann, J., & White, S. D. M. 2006, *MNRAS*, 370, 1106
- Gandhi, P., Horst, H., Smette, A., et al. 2009, *A&A*, 502, 457
- Geier, S., Richard, R., Man, A. W. S., et al. 2013, *ApJ*, 777, 87
- Gilli, R., Norman, C., Vignali, C., et al. 2014, *A&A*, 562, 67
- Goldoni, P. 2011, *AN*, 332, 227
- Graham, A. W., & Driver, S. P. 2007, *ApJ*, 655, 77
- Gültekin, K., Richstone, D. O., Mo, H. J., et al. 2009, *MNRAS*, 398, 1129
- Hainline, K. N., Shapley, A. E., Greene, J. E., et al. 2011, *ApJ*, 733, 31
- Hall, P. B., Hoversten, E. A., Tremonti, C. A., et al. 2004, *AJ*, 128, 3148
- Hao, L., Strauss, M. A., Fan, X., et al. 2005, *AJ*, 129, 1783
- Harrison, F. A., Craig, W. W., Christensen, F. E., et al. 2013, *ApJ*, 770, 103
- Holden, B. P., Oesch, P. A., Gonzalez, V. G., et al. 2014, *ApJ*, submitted
- Hopkins, P. F., Richards, G. T., Hernquist, L. 2007, *ApJ*, 654, 731
- Hopkins, P. F., Hernquist, L., Cox, T. J., Keres, D. 2008, *ApJS*, 175, 356
- Horne, K. 1986, *PASP*, 98, 609
- Ilbert, O., Capak, P., Salvato, M., et al. 2009, *ApJ*, 690, 1236
- Juneau, S., Dickinson, M., Alexander, D. M., & Salim, S. 2011, *ApJ*, 736, 104
- Juneau, S., Bournaud, F., Charlot, S., et al. 2014, *ApJ*, accepted
- Kauffmann, G., & White, S.D.M. 1993, *MNRAS*, 261, 921
- Kauffmann, G., Colberg, J.M., Diaferio, A., et al. (1999), *MNRAS*, 307, 529
- Kauffmann, G., Haehnel, M. 2000, *MNRAS*, 311, 576
- Kennicutt, Jr., R. C. 1998, *ARA&A*, 36, 189
- Kewley, L. J., Groves, B., Kauffmann, G., & Heckman, T. 2006, *ApJ*, 372, 961
- Kirkpatrick, A., Pope, A., Alexander, D. M., et al. 2012, *ApJ*, 759, 139
- Koekemoer, A. M., Fruchter, A. S., Hook, R. N., & Hack, W. 2002, in *The 2002 HST Calibration Workshop*, ed. S. Arribas
- Kriek, M., van Dokkum, P. G., Labbé, I., et al. 2009, *ApJ*, 700, 221
- Kroupa, P. 2001, *MNRAS*, 322, 231
- Kuiper, E., Hatch, N. A., Miley, G. K., et al. 2011, *MNRAS*, 415, 2245
- Kulas, K. R., Shapley, A. E., Kollmeier, J. A., et al. 2012, *ApJ*, 754, 33
- Kummel, M., Walsh, J. R., Pirzkal, N., et al. 2009, *PASP*, 121, 875
- Kummel, M., Rosati, P., Fosbury, R., et al. 2011, *A&A*, 530, 86
- Labbé, I., Huang, J., Franx, M., et al. 2005, *ApJ*, 624, L81
- Lamastra, A., Bianchi, S., Matt, G., et al. 2009, *A&A*, 504, 73
- Mancini, C., Matute, I., Cimatti, A., et al. 2009, *A&A*, 500, 705
- Maraston, C. 2005, *MNRAS*, 362, 799
- Marchesini, D., van Dokkum, P. G., Föster Schreiber, N. M., Franx, M., Labbé, I., & Wuyts, S. 2009, *ApJ*, 701, 1765
- Marchesini, D., Whitaker, K. E., Brammer, G., et al. 2010, *ApJ*, 725, 1277
- Marchesini, D., Muzzin, A., Stefanon, M., et al. 2014, *ApJ*, submitted
- Marconi, A., Risaliti, G., Gilli, R., et al. 2004, *MNRAS*, 351, 169
- Martin, D. C., et al. 2005, *ApJ*, 619, L1
- Maschietto, F., Hatch, N. A., Venemans, B. P., et al. 2008, *MNRAS*, 389, 1223
- McCracken, H. J., et al. 2010, *ApJ*, 708, 202
- McLean, I. S., Becklin, E. E., Bendiksen, O., et al. 1998, *SPIE*, 3354, 566
- McLinden, E., Finkelstein, S. L., Rhoads, J. E., et al. 2011, *ApJ*, 730, 136
- Mendel, J. T., Simard, L., Ellison, S. L., & Patton, D. R. 2013, *MNRAS*, 429, 2212
- Mihos, J. C., & Hernquist, L. 1994, *ApJ*, 425, L13
- Modigliani, A., Goldoni, P., Royer, F., et al. 2010, *Proc. SPIE*, 7737, 56
- Mullaney, J. R., Alexander, D. M., Fine, S., et al. 2013, *MNRAS*, 433, 622
- Muzzin, A., Marchesini, D., Stefanon, M., et al. 2013, *ApJS*, 206, 8
- Muzzin, A., Marchesini, D., Stefanon, M., et al. 2013, *ApJ*, 777, 18
- Naab, T., Khochfar, S., & Burkert, A., 2006, *ApJ*, 636, L81
- Nakajima, K., Ouchi, M., Shimasaku, K., et al. 2013, *ApJ*, 769, 3
- Nandra, K., & Pounds, K. A. 1994, *MNRAS*, 268, 405
- Norman, C., Hasinger, G., Giacconi, R., et al. 2002, *ApJ*, 571, 218
- Patel, S. G., Holden, B. P., Kelson, D. D., et al. 2012, *ApJ*, 748, L27
- Patel, S. G., van Dokkum, P. G., Franx, M., et al. 2013, *ApJ*, 766, 15
- Peng, C. Y., Ho, L. C., Impey, C. D., et al. 2002, *ApJ*, 124, 266
- Peng, C. Y., Impey, C. D., Rix, H.-W., et al. 2006, *ApJ*, 649, 616
- Pérez-González, P.G., Rieke, G.H., Villar, V., et al. 2008, *ApJ*, 675, 234
- Pettini, M., Shapley, A. E., Steidel, C. C., et al. 2001, *ApJ*, 554, 981
- Polletta, M., Tajer, M., Maraschi, L., et al. 2007, *ApJ*, 663, 81
- Rawlings, S., & Saunders, R. 1991, *Nature*, 349, 138
- Ricciardelli, E., Trujillo, I., Buitrago, F., & Conselice, C. J. 2010, *MNRAS*, 406, 230
- Richards, G. T., Kruczek, N. E., Gallagher, S. C., et al. 2011, *ApJ*, 141, 167
- Salpeter, E. 1955, *ApJ*, 121, 161
- Sanders, D. B., Salvato, M., Aussel, H., et al. 2007, *ApJS*, 172, 86
- Schinnerer, E., Smolčić, V., Carilli, C. L., et al. 2007, *ApJS*, 172, 46
- Scoville, N., Aussel, H., Brusa, M., et al. 2007, *ApJS*, 172, 1
- Scudder, J. M., Ellison, S. L., Torrey, P., et al. 2012, *MNRAS*, 426, 549
- Silverman, J. D., Lamareille, F., Maier, C., et al. 2009, *ApJ*, 696, 396
- Skilton, R. E., Whitaker, K. E., Momcheva, I. G., et al. 2014, *ApJS*, submitted
- Spoon, H. W. W., Farrah, D., Leboutellier, V., et al. 2013, *ApJ*, 775, 127
- Straatman, C. M. S., Labbé, I., Spitler, L. R., et al. 2014, *ApJ*, 783, L14
- Stefanon, M., Marchesini, D., Rudnick, D., et al. 2013, *ApJ*, 768, 92
- Taniguchi, Y., et al. 2007, *ApJS*, 172, 9
- Teplitz, H. I., McLean, I. S., Becklin, E. E., et al. 2000, *ApJ*, 533, L65
- Thomas, D., Maraston, C., Bender, R., & Mendes de Oliveira, C. 2005, *ApJ*, 621, 673
- Thomas, D., Maraston, C., Schawinski, K., Sarzi, M., & Silk, J. 2010, *MNRAS*, 404, 1775
- Toft, S., van Dokkum, P., Franx, M., et al. 2007, *ApJ*, 671, 285
- Tremonti, C. A., Heckman, T. M., Kauffmann, G., et al. 2004, *ApJ*, 613, 898
- Trujillo, I., Feulner, G., Goranova, Y., et al. 2006, *MNRAS*, 373, 36
- Trujillo, I., Conselice, C. J., Bundy, K., et al. 2007, *MNRAS*, 381, 109
- Trujillo, I., Ferreras, I., de La Rosa, I. G., 2011, *MNRAS*, 415, 3903
- Valdes, F., ASPC, 25, 417
- Van De Sande, J., Kriek, M., Franx, M., et al. 2013, *ApJ*, 771, 85
- van de Voort, F., Schaye, J., Booth, C. M., et al. 2011, *MNRAS*, 415, 2782
- van der Wel, A., Holden, B.P., Zirm, A.W., et al. 2008, *ApJ*, 688, 48
- van der Wel, A., et al. 2014, *ApJ* submitted [arXiv:1404.2844]
- van Dokkum P. G., 2001, *PASP*, 113, 1420
- van Dokkum P. G., & Stanford, S. A. 2003, *ApJ*, 585, 78
- van Dokkum, P. G., Franx, M., Kriek, M., et al. 2008, *ApJ*, 677, 5
- van Dokkum, P. G., Labbé, I., Marchesini, D., et al. 2009, *PASP*, 121, 2
- van Dokkum, P. G., Whitaker, K., Brammer, G., et al. 2010, *ApJ*, 709, 1018
- van Dokkum, P. G., Brammer, G., Fumagalli, M. et al. 2011, *ApJ*, 743L, 15
- Verhamme, A., Schaerer, D., & Maselli, A. 2006, *A&A*, 460, 397
- Wake, D. A., van Dokkum, P. G., & Franx, M. 2012, *ApJ*, 751, L44
- Weinzirl, T., Jogee, S., Conselice, C. J., et al. 2011, *ApJ*, 743, 87
- Wiklund, T., Dickinson, M., Ferguson, H. C., et al. 2008, *ApJ*, 676, 781
- Williams, R. J., Quadri, R. F., Franx, M., et al. 2009, *ApJ*, 691, 1879
- Whitaker, K. E., Labbé, I., van Dokkum, P. G., et al. 2011, *ApJ*, 735, 86
- White, S.D., & Frenk, C.S., 1991, *ApJ*, 379, 52
- White, S.D., & Rees, M.J., 1978, *MNRAS*, 183, 341
- Williams, C. C., et al. 2014, *ApJ*, 780, 1
- Wuyts, S., Labbé, I., Franx, M., et al. 2007, *ApJ*, 655, 51
- Wuyts, S., Förster Schreiber, N. M., Lutz, D., et al. 2011, *ApJ*, 738, 106
- Zirm, A.W., van der Wel, A., Franx, M., et al. 2007, *ApJ*, 656, 66